8 LARGE EXTRA DIMENSIONS

8.1 Introduction

Daniele Dominici and Samir Ferrag

Recent theories with extra dimensions are an attempt to understand the large difference between the Planck mass M_{Pl} and the Fermi scale $G_F^{-1/2}$ through a geometrical reformulation of the gauge hierarchy problem. In general these theories are formulated in a D-dimensional space time which has the geometry of a direct product $\mathcal{M}^4 \times X^\delta$ where $\mathcal{M}^4$ denotes the Minkowski space and X^δ the internal (compact) space [1, 2] but also non factorizable metrics and non compact spaces have been considered [3, 4]. In the large extra dimension models [1, 2] non gravitational interactions are confined to a 4-dimensional space time (the brane) while the gravitational interactions propagate in $D = 4 + \delta$ dimensions (the bulk). The standard Planck mass becomes an effective parameter and it is replaced by a fundamental parameter $\overline{M}_D$ which is of the order of a TeV. The big hierarchy between $\overline{M}_D$ and the Planck mass is explained by the large compactification volume V_δ appearing in the formula:

$$\overline{M}_{Pl}{}^2 = V_\delta \overline{M}_D{}^{2+\delta} \tag{8.1}$$

where $\overline{M}_{Pl} = 1/\sqrt{8\pi G_N} = 2.4 \times 10^{18}$GeV is the reduced Planck mass. Assuming as internal space a δ-torus with a common radius R, the compactification volume is given by $V_\delta = (2\pi R)^\delta$. The case $\delta = 1$ is excluded because it would give modifications to the Newton law at solar system distances; however for $\delta = 2$, assuming $\overline{M}_D = 1$ TeV, we can explain the large separation between the Planck and the electroweak scale with a radius $R \lesssim 10^{-2}$ mm, which is below the present limits on large extra dimensions from Newton law deviation experiments (200 μm) [5].

If the scale of the additional dimensions is small enough ($\leq$ TeV^{-1}) then also electroweak and strong interactions can propagate in the bulk. The existence of TeV sized compact extra dimensions has been also suggested for different reasons, related to the possibility of breaking supersymmetry [6] or a gauge symmetry by boundary conditions [7, 8] or explaining fermion mass spectrum delocalizing quarks and leptons in different regions of the extra dimensions [9]. This has motivated the construction of extensions of the Standard Model (SM), without gravity, in five or more dimensions, with matter and scalar fields living on branes or delocalized in the bulk. In the simplest version, known as Universal Extra Dimensions (UED) [10], all fields live in the bulk. These models are of interest because for the presence of a conserved Z_2 symmetry, which is a subgroup of the translation invariance in the fifth dimension, they are only weakly constrained by the electroweak precision measurements (for a recent analysis, see [11]). Furthermore for the same Z_2 symmetry the lightest Kaluza-Klein (KK) mode is stable and provides a candidate for dark matter [12, 13]. Models where matter and/or Higgses live on branes are more constrained by the electroweak precision measurements: 95% CL lower bound on the compactification scale are $M = 1/R \sim 5 - 6$ TeV [14–21].

All these higher dimensional theories are non renormalizable and therefore they should be interpreted as low energy effective theories valid up to some cut-off scale where some ultraviolet completion is necessary.

8.1.1 Review of the Arkani-Hamed-Dimopoulos-Dvali (ADD) model

The action of the theory is given by the $D = 4+\delta$ dimensional Einstein term and a brane term containing the SM gauge interactions [22, 23]:

$$S = \frac{\overline{M}_D{}^{2+\delta}}{2} \int d^D x \sqrt{|g|} R + \int d^4 x \sqrt{-g_{\rm ind}} \mathcal{L}_{\rm SM} \tag{8.2}$$

where $R = g^{AB} R_{AB}$, $(A, B = 0, \cdots, 3+\delta)$ is the Ricci scalar curvature in D dimensions and $(g_{\rm ind})_{\mu\nu}$ is the metric induced on the brane. If the internal space is a δ-torus, $\int d^D x = \int d^4 x \int_0^{2\pi R} dy_1 \cdots \int_0^{2\pi R} dy_\delta$.

The action is computed by performing a linear expansion for weak gravity:

$$g_{AB} = \eta_{AB} + \frac{2}{\overline{M}_D{}^{1+\delta/2}} h_{AB} \tag{8.3}$$

up to second order in the fields h_{AB} and expanding h_{AB} in Fourier series:

$$h_{AB} = \sum_{n_1=-\infty}^{+\infty} \cdots \sum_{n_\delta=-\infty}^{+\infty} \frac{1}{\sqrt{V_\delta}} h_{AB}^{(n)}(x) e^{-i\sum_{j=1}^{\delta} n_j y_j} \tag{8.4}$$

where the KK modes $h_{AB}^{(n)}$ appear:

$$h_{AB}^{(n)} = \begin{pmatrix} h_{\mu\nu}^{(n)} & h_{\mu j}^{(n)} \\ h_{i\nu}^{(n)} & h_{ij}^{(n)} \end{pmatrix} \tag{8.5}$$

where $\mu, \nu = 0, 1, 2, 3$ and $i, j = 1, \cdots, \delta$.

The quadratic Lagrangian can be re-expressed in the unitary gauge as

$$\begin{aligned} \mathcal{L} \;=\; & \sum_{\vec{n}} \Big[-\frac{1}{2} G^{(-\vec{n})\mu\nu} (\Box + m_n^2) G_{\mu\nu}^{(\vec{n})} + \frac{1}{2} G_\mu^{(-\vec{n})\mu} (\Box + m_n^2) G_\mu^{(\vec{n})\mu} \\ & - G^{(-\vec{n})\mu\nu} \partial_\mu \partial_\nu G_\lambda^{(\vec{n})\lambda} + G^{(-\vec{n})\mu\nu} \partial_\mu \partial_\lambda G_\nu^{(\vec{n})\lambda} \\ & - \frac{1}{4} |\partial_\mu V_{\nu j}^{(\vec{n})} - \partial_\nu V_{\mu j}^{(\vec{n})}|^2 + \frac{1}{2} m_n^2 V_{\mu j}^{(-\vec{n})} V^{(\vec{n})\mu j} - \frac{1}{2} S^{(-\vec{n})jk} (\Box + m_n^2) S_{jk}^{(\vec{n})} \\ & - \frac{1}{2} H^{(-\vec{n})} (\Box + m_n^2) H^{(\vec{n})} \Big] \end{aligned} \tag{8.6}$$

where $G_{\mu\nu}^{(\vec{n})}$, $V_{\mu j}^{(\vec{n})}$, $S_{jk}^{(\vec{n})}$ and $H^{(\vec{n})}$ are suitable linear combinations of the fields appearing in Eq. (8.5) [22, 23] and where the mass of the Kaluza-Klein excitations is given by

$$m_n = \frac{|\vec{n}|}{R} \tag{8.7}$$

Assuming again $\delta = 2$, and $\overline{M}_D = 1$ TeV, the range of the masses is of order 10^2 mm$^{-1} \sim 10^{-1}$ eV. Therefore in large extra dimension models KK gravitons tend to be very light and densely spaced ($\Delta m_n \sim 1/R$). Finally the brane action, when computed using the Fourier expansion, gives the following interaction Lagrangian

$$-\frac{1}{\overline{M}_{Pl}} \sum_{\vec{n}} \Big[G^{(\vec{n})\mu\nu} - \frac{\kappa}{3} \eta^{\mu\nu} H^{(\vec{n})} \Big] T_{\mu\nu} \tag{8.8}$$

where $\kappa = \sqrt{\frac{3(\delta-1)}{\delta+2}}$ and $T_{\mu\nu}$ is the energy momentum tensor built from the SM Lagrangian, $\mathcal{L}_{SM}$. Notice that the vectors $V_{\mu j}^{(\vec{n})}$ and the scalars $S_{jk}^{(\vec{n})}$ do not couple to the ordinary matter. A mechanism for generating a small mass (≥ 1 mm$^{-1} \sim 10^{-3}$ eV) for the zero mode of the scalar fields $H^{(\vec{n})}$ is necessary in order to avoid deviations to the Newton law at the corresponding scale of 1 mm [24].

Feynman rules for the massive gravitons $G_{\mu\nu}^{(\vec{n})}$ and for the graviscalars $H^{(\vec{n})}$ can be derived from Eqs. (8.6)–(8.8) and are contained in [22, 23]. Since the couplings of these particles to ordinary matter are $O(1/\overline{M}_{Pl})$ their life-times tend to be very long. On the other side, even if their couplings are weak, the inclusive KK production cross section can be large at energies close to $\overline{M}_D$ because of the large multiplicity of the final state. In order to quantify this argument, let us consider the density of states: the number of modes $dN(|\vec{n}|)$ with the modulus $|\vec{n}| \equiv |n|$ being in the interval $(|n|, |n| + d|n|)$ is given by

$$dN(|\vec{n}|) = S_{\delta-1} |n|^{\delta-1} d|n| = S_{\delta-1} R^\delta m^{\delta-1} dm \tag{8.9}$$

Table 8.1: 95% CL bounds on M_D (TeV)

δ	2	3	4	5	6
95% CL collider bounds on M_D (TeV)					
LEP Exotica WG [25]	1.60	1.20	0.94	0.77	0.66
D0 mono-jets Run I data (K=1) [26]	0.89	0.73	0.68	0.64	0.63
CDF mono-jets Run I data (K=1) [27]	1.00		0.77		0.71
Astrophysical bounds on M_D (TeV)					
SN1987A [28, 29]	22	2			
Diffuse γ rays from SN/NS [28, 29]	97	8	1.5		
Excess heat from γ hitting the NS [28, 29]	1800	77	9.4	2.1	

with $m \equiv m_n = |n|/R$ and where $S_{\delta-1} = 2\pi^{\delta/2}/\Gamma(\delta/2)$ is the surface of the unit sphere in δ dimensions. We evaluate the sum over the KK excitations by converting it in the continuum notation

$$\begin{aligned} \sum_{\vec{n}} \;\; &\rightarrow \;\; \int dm^2 \rho_\delta(m) \\ &= \frac{1}{2} \frac{\overline{M}_{Pl}{}^2}{M_D^{2+\delta}} S_{\delta-1} \int dm^2 m^{\delta-2} \end{aligned} \tag{8.10}$$

It turns out that the density of states is

$$\rho_\delta(m) = \frac{L^\delta m^{\delta-2}}{(4\pi)^{\delta/2}\Gamma(\delta/2)} = \frac{\overline{M}_{Pl}{}^2}{2M_D^{2+\delta}} S_{\delta-1} m^{\delta-2} \tag{8.11}$$

where we have used $L = 2\pi R$ and we have defined a new effective D-dimensional Planck mass

$$M_D = (2\pi)^{\frac{\delta}{\delta+2}} \overline{M}_D \tag{8.12}$$

such that $1/(8\pi G_N) = R^\delta M_D^{\delta+2}$.

LEP has searched for graviton production in the process $e^+e^- \rightarrow \gamma(Z) + \text{missing energy}$. The corresponding 95% CL lower limits on M_D, using the best channel (γ plus missing energy), are shown in Table 8.1 [25]. The Tevatron 95% CL limits on M_D using the missing energy plus a single jet process are shown in Table 8.1 [26, 27] . LEP results are more sensitive for small extra dimensions. Some preliminary results of Run II have been presented for D0 [30].

As shown in Table 8.1, strong astrophysical bounds from supernova and neutron star processes involving emission of KK gravitons are present for $\delta \leq 3$ [28, 29]. However, as suggested [31], while astrophysics probes only the infrared part of the Kaluza-Klein spectrum of gravitons, high-energy experiments are mainly sensitive to the ultraviolet part. These limits can be evaded by assuming a small distortion of the D-dimensional space so that the mass of the lightest KK excitation is not given by the inverse radius $1/R$, but by a new intrinsic mass μ. If $\mu \simeq 50$ MeV gravitons cannot be produced in astrophysical systems and therefore no bounds on the scale M_D are derived. This idea has been pursuit also to study the case corresponding to $\delta = 1$ [31]. The model is built using the Randall Sundrum metric [3] (see also Section 9) but assuming the visible brane at $y = 0$ and the Planck brane at $y = \pi R$, in the limit in which μ is larger than R^{-1} and both are much smaller than $\bar{M}_5$. In this model the hierarchy between the Fermi and the Planck scale is explained both by the warp factor and by the large extra dimension.

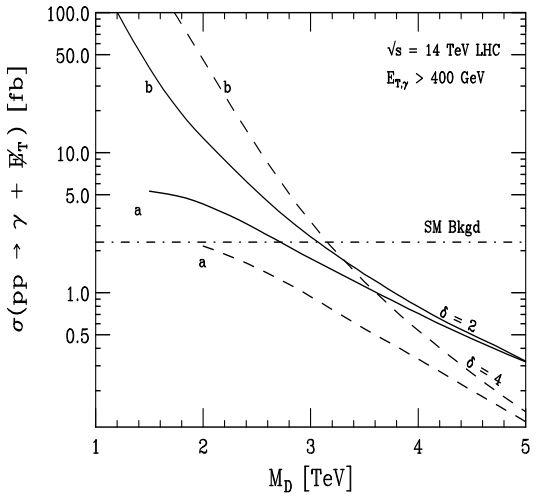

Fig. 8.1: $\gamma + \not{E}_T$ cross sections after integrating over a) $\hat{s} < M_D^2$ or b) all $\hat{s}$, where $\hat{s}$ is subprocess s. The SM background is the dot-dashed line. The signal is plotted as a solid (dashed) line for $\delta = 2(4)$. Taken from [32].

8.1.2 Direct graviton production

The process which are relevant for LHC are the production of jets plus missing energy and photon plus missing energy. They are associated with the amplitudes $gg \to gG^{(\vec{n})}$, $qG \to qG^{(\vec{n})}$, $q\bar{q} \to gG^{(\vec{n})}$ and $q\bar{q} \to \gamma G^{(\vec{n})}$ respectively.

The relevant partonic differential cross section for single graviton emission $d^2\sigma/dtdm$ is proportional to the coupling $\sim 1/\overline{M}_{Pl}^2$ (as seen from Eq. (8.8)), however, summing over all the KK gravitons and taking into account the final state density, Eq. (8.11), the final form for the differential cross section is proportional to $1/M_D^{\delta+2}$. Figure 8.1 shows the total cross section for the final state photon plus missing energy for the signal for $\delta = 2, 4$ and for the SM background. This channel is less sensitive than the jet plus missing energy one, because of the smallness of the electromagnetic coupling and the lower luminosity of $q\bar{q}$ with respect to qg. Figure 8.2 shows the missing transverse energy distribution of the backgrounds and of the signals for several choices of δ and M_D for the channel jet plus missing energy. The signals have been generated using the ISAJET implementation of the extra dimension model and the fast simulation of the ATLAS detector (ATLFAST) has been used. At the large values of missing transverse energy the dominant backgrounds arise from processes that can give rise to neutrinos in the final state, jet $+Z(\to \nu\nu)$, jet $+W(\to l\nu)$. The sensitivity for $\delta = 2, 3$ and 4 is respectively $M_D = 9.1, 7.0$ and 6.0 TeV for 100 fb^{-1} [33]. For comparison we report here also the sensitivity of ILC with $\sqrt{s} = 800$ GeV, integrated luminosity $L = 1$ ab^{-1}, from the channel $e^+e^- \to \gamma G^{(\vec{n})}$: the 95% CL limits are M_D=5.9, 3.5 and 2.5 TeV for $\delta = 2$, 4 and 6 TeV respectively for unpolarized beams and 10.4, 5.1 and 3.3 TeV for $P_- = 0.8$, $P_+ = 0.6$ [34]. As shown in Fig. 8.3, the evolution of the $e^+e^- \to \gamma \not{E}_T$ cross section with the center of mass energy of the linear collider depends strongly on the number of extra dimensions [35]. Measurements of cross sections at different energies, as shown in [36], can determine the values of M_D and δ. Drell–Yan lepton pairs plus missing energy [37] have been also considered however the corresponding reach is lower than the single jet process.

The model corresponding to $\delta = 1$ has been recently studied in [31] by considering a warping of the 5-dimensional metric. The warping avoids standard conflicts with observations by introducing a mass gap in the KK graviton spectrum. LHC can be sensitive up to $M_D = 17$ TeV for 100 fb^{-1}.

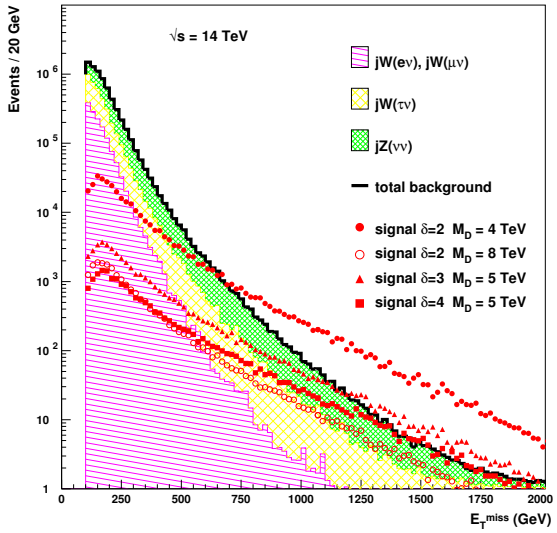

Fig. 8.2: Missing energy distribution (dots), shown here for various choices of the number of extra dimensions (δ) and of the mass scale (M_D) and for SM backgrounds (histograms) for the channel jet $+\not{E}_T$. Taken from [33].

8.1.3 Virtual graviton exchange

The graviton, or any of its KK modes, can be exchanged in the s-channel. The multiplicity of KK states can give a large contribution to the production cross sections of any final state and the cross sections are divergent for $\delta \geq 2$. The expression of the cross section have been regularized in [23] by cutting off all the KK contributions above M_S where M_S presumably is of order M_D. The first ATLAS study [38] focused on the channels $pp \to l^+l^- + X$ and $pp \to \gamma\gamma + X$. Fig. 8.4 shows the signal shape for the two channels as a function of the two final state particle invariant mass. For a luminosity of 100 fb^{-1} (one year of LHC at high luminosity) and combining the two channels, a 5σ sensitivity to an energy scale M_S of 7 to 8 TeV is reached for a number of extra dimensions varying between 2 and 5.

In the simulations for the ILC the exchange of KK gravitons has been approximated by the following dimension eight operator:

$$\mathcal{L} = i\frac{4\lambda}{\Lambda^4}T^{\mu\nu}T_{\mu\nu} \tag{8.13}$$

where $|\lambda| = 1$ and Λ is a cut-off related to M_S. Deviations with respect to the SM in fermion and $\gamma\gamma$ channels, left-right and center-edge asymmetries have been investigated [22, 39–43]. 5σ sensitivity for $\sqrt{s} = 500(1000)$ GeV and integrated luminosity of 500 fb^{-1} turns out to be $\Lambda = 3.5$ (5.8) TeV [44]. The corresponding analysis for CLIC [45] gives a limit $M_S \sim 6\sqrt{s}$ for an integrated luminosity of 1 ab^{-1}.

8.1.4 Invisible Higgs decay

An entirely different class of signals is associated with the mixing between the Higgs boson and the very dense (continuum-like) graviscalar states. Instead of a single Higgs boson, one must consider the production of the full set of densely spaced mass eigenstates all of which are mixing with one another. The new signature that arises as a result of this mixing is that the Higgs boson will effectively acquire a possibly very large branching ratio to invisible final states composed primarily of graviscalars [32,46,47]. If the Higgs-graviscalar mixing parameter is of order one, then the Higgs decays to invisible final states will provide invaluable probes of the ADD model, often allowing detection of the extra dimensions in portions of parameter space for which the $jets/\gamma + \not{E}_T$ signal is not observable. If both types of signal are observable, a complete determination of the model parameters is generally possible [36]. The

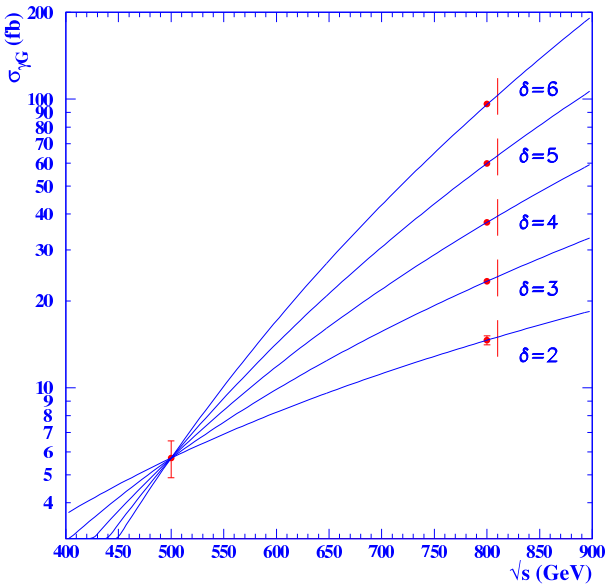

Fig. 8.3: $\gamma + \not{E}_T$ cross sections vs. $\sqrt{s}$, normalized to a common value at $\sqrt{s} = 500$ GeV. Thus, energy dependence gives δ via ratio of cross sections. Absolute normalization then gives M_D. Taken from [35].

interaction between the Higgs complex doublet field H and the Ricci scalar curvature R of the induced 4-dimensional metric $g_{\rm ind}$ is derived from the following action

$$S = -\xi \int d^4x \sqrt{-g_{\rm ind}} R(g_{\rm ind}) \Phi^\dagger \Phi \,. \tag{8.14}$$

After the usual shift $\Phi = (v + \frac{h}{\sqrt{2}}, 0)$, this interaction leads to the mixing term [32], (we have rewritten the graviscalars $H^{(\vec{n})} = 1/\sqrt{2}(s_{\vec{n}} + i a_{\vec{n}})$)

$$\mathcal{L}_{\rm mix} = \epsilon h \sum_{\vec{n}>0} s_{\vec{n}} \tag{8.15}$$

with

$$\epsilon = -\frac{2\sqrt{2}}{\overline{M}_{Pl}} \xi v m_h^2 \sqrt{\frac{3(\delta-1)}{\delta+2}} \,. \tag{8.16}$$

This mixing generates an oscillation of the Higgs itself into the closest KK graviscalar levels which decay invisibly. The invisible width $\Gamma_{h\to invisible} \equiv \Gamma_{inv}$ can be calculated by extracting the imaginary part of the mixing contribution to the Higgs self energy [32]. In an equivalent way the mixing requires diagonalization to the physical eigenstates h' and $s'_{\vec{n}}$: the $s'_{\vec{n}}$ are nearly continuous and so those near in mass to the h' act coherently together with the h'. Then when computing a process such as $WW \to h' + \sum_{\vec{m}>0} s'_{\vec{m}} \to F$, the full coherent sum over physical states must be performed. The result at the amplitude level is

$$\mathcal{A}(WW \to F)(p^2) \sim \frac{g_{WWh} g_{hF}}{p^2 - m_h^2 + i m_h \Gamma_h + i G(p^2) + F(p^2) + i\bar{\epsilon}} \tag{8.17}$$

where $\bar{\epsilon}$ provides the standard Feynman prescription and

$$F(p^2) \equiv -\epsilon^2 {\rm Re}\left[\sum_{\vec{m}>0} \frac{1}{p^2 - m_{\vec{m}}^2 + i\bar{\epsilon}}\right], \quad G(p^2) \equiv -\epsilon^2 {\rm Im}\left[\sum_{\vec{m}>0} \frac{1}{p^2 - m_{\vec{m}}^2 + i\bar{\epsilon}}\right] \tag{8.18}$$

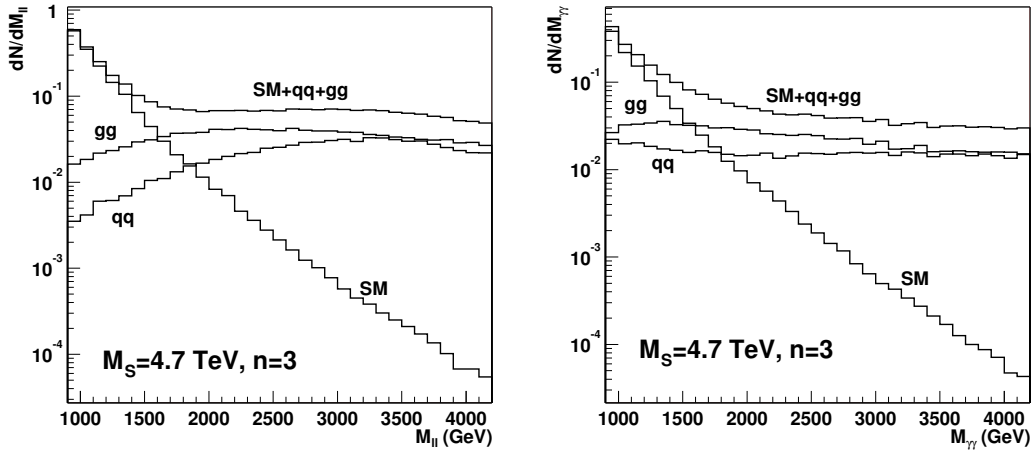

Fig. 8.4: Left: $pp \to l^+l^-$ cross section versus di-lepton invariant mass for SM and for 3 extra-dimensions with $M_S = 4.7$ TeV. Labeled contributions $q\bar{q}$ or gg correspond to a graviton exchange with $q\bar{q}$ or gg initial state. Right: same for $pp \to \gamma\gamma$. Taken from [38].

Writing $F(p^2) = F(m_{h^2_{eff}}) + (p^2 - m_{h^2_{eff}})F'(m_{h^2_{eff}}) + \ldots$, where $m_{h^2_{eff}} - m_h^2 + F(m_{h^2_{eff}}) = 0$, we obtain the structure

$$\mathcal{A}(WW \to F)(p^2) \sim \frac{g_{WWh} g_{hF}}{(p^2 - m_{h^2_{eff}})[1 + F'(m_{h^2_{eff}})] + i m_h(\Gamma_h + \Gamma_{inv})} \tag{8.19}$$

with

$$m_h \Gamma_{inv} = G(p^2)|_{m_{h^2_{eff}}} = Im\Sigma(p^2)|_{m_{h^2_{eff}}} \tag{8.20}$$

A simple estimate of the mass renormalization is that $F(m^2_{h_{eff}})$ should be of order $\xi^2 m_h^6/\Lambda^4$, where Λ is an unknown ultraviolet cutoff energy presumably of order $\Lambda \sim M_D$ [22]. In this case, the contribution from $F(m^2_{h_{eff}})$ is small for $m_h \ll M_D$. A simple estimate of the quantity $F'(m^2_{h_{eff}})$, associated with wave function renormalization, suggests that it is of order $\xi^2 \frac{m_h^4}{\Lambda^4}$. In this case, F' will provide a correction to coherently computed LHC production cross sections that is very probably quite small for $m_h \ll M_D$. Neglecting the terms F, F', then $m_{h_{eff}} \sim m_h$. Taking the amplitude squared and integrating over dp^2 in the narrow width approximation we get

$$\sigma(WW \to h' + \sum_{\vec{n}>0} s_{\vec{n}} \to F) = \sigma_{SM}(WW \to h \to F) \times \left[\frac{\Gamma^{SM}_{h\to F}}{\Gamma^{SM}_h + \Gamma_{inv}}\right] \tag{8.21}$$

with

$$\begin{aligned} m_h \Gamma_{inv} = G({m_h}^2) \qquad &\to -\epsilon^2 Im \frac{1}{2} \int d{m}^2 \rho_\delta(m) \frac{1}{{m_h}^2 - m^2 + i\bar{\epsilon}} \\ &= -\epsilon^2 \frac{1}{4} \frac{\overline{M}_P^2}{M_D^{2+\delta}} S_{\delta-1}(-\pi)({m_h}^2)^{(\delta-2)/2} \end{aligned} \tag{8.22}$$

So finally

$$\begin{aligned} \Gamma_{inv} = 2\pi\xi^2 v^2 \frac{3(\delta-1)}{\delta+2} \frac{m_h^{1+\delta}}{M_D^{2+\delta}} S_{\delta-1} \quad &\sim \quad (16\,MeV) 20^{2-\delta} \xi^2 S_{\delta-1} \frac{3(\delta-1)}{\delta+2} \\ &\times \left(\frac{m_h}{150\,\mathrm{GeV}}\right)^{1+\delta} \left(\frac{3\,\mathrm{TeV}}{M_D}\right)^{2+\delta} \end{aligned} \tag{8.23}$$

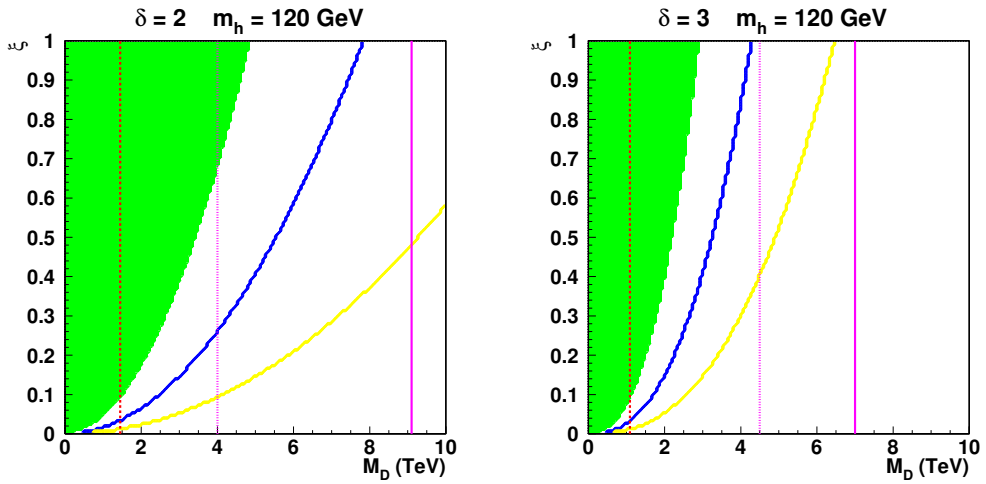

Fig. 8.5: Invisible decay width effects in the ξ - M_D plane for m_h = 120 GeV. The plots are for $\delta = 2$ (left), 3 (right). The green (grey) regions indicate where the Higgs signal at the LHC drops below the 5σ threshold for 100 fb^{-1} of data. The regions above the blue (bold) line are where the LHC invisible Higgs signal in the WW-fusion channel exceeds 5σ significance. The solid vertical line at the largest M_D value in each figure shows the upper limit on M_D at the 5σ level by the analysis of jets/γ with missing energy at the LHC. The middle dotted vertical line shows the value of M_D below which the theoretical computation at the LHC is ambiguous. The dashed vertical line at the lowest M_D value is the 95% CL lower limit coming from combined Tevatron and LEP/LEP2 limits. The regions above the yellow (light grey) line are the parts of the parameter space where the ILC invisible Higgs signal will exceed 5σ assuming $\sqrt{s} = 350$ GeV and $L = 500$ fb^{-1}. Taken from [36].

In the ADD model, the statistical significance for detecting a SM Higgs in the standard visible channels is suppressed by the appearance of this invisible decay width. There are regions at high ξ where the significance of the Higgs boson signal in the canonical channels drops below the 5σ threshold. Fortunately, the LHC experiments will also be sensitive to an invisibly decaying Higgs boson produced via WW-fusion, with tagged forward jets. In Ref. [48] the results of a detailed CMS study for this mode are given in Fig. 25, (see also Fig. 8.10). With only 10 fb^{-1}, a Higgs boson produced with the SM WW →Higgs rate and decaying to an invisible final state with $BR(h \to invisible) = 0.12 - 0.28$ exceeds the 95% CL for 120 GeV $< m_h <$ 400 GeV. Fig. 8.5 summarizes the results for different values of δ when $m_h = 120$ GeV. In the green (light grey) region, the Higgs signal in standard channels drops below the 5σ threshold with 100 fb^{-1} of LHC data. But in the area above the bold blue line the LHC search for invisible decays in the fusion channel yields a signal with an estimated significance exceeding 5σ. It is important to observe that, whenever the Higgs boson sensitivity is lost due to the suppression of the canonical decay modes, the invisible rate is large enough to still ensure detection through a dedicated analysis. For increasing m_h the invisible decay mode is important in a more limited range because the SM Higgs decay width is much larger in this latter case, m_h being above the WW, ZZ pair decay thresholds.

The 5σ upper reach in M_D at each δ from the analysis of jets/γ+ missing energy [33] is shown in the figures by the solid medium gray (purple) line. The reliability of the theory prediction at the LHC fails for M_D below the medium gray (purple) dotted line. Also shown in each figure is the 95% CL lower limit on M_D coming from the combination of LEP, LEP2 and Tevatron data, as summarized in [49]. A TeV-class e^+e^- linear collider will be able to see the Higgs signal regardless of the magnitude of the invisible branching ratio simply by looking for a peak in the M_X mass spectrum in $e^+e^- \to ZX$ events. We should note that the $e^+e^- \to Z\not{E}_T$ events from direct graviton emission do not result in substantial background [50] to the Higgs signal when $\sqrt{s} \lesssim 500$ GeV. The region above the light grey (yellow)

curves in Fig. 8.5 corresponds to the portion of (M_D, ξ) parameter space for which the invisible Higgs signal will be observable at the ILC at the 5σ or better level. Not surprisingly, the ILC will be able to detect this signal over an even larger part of the parameter space than can the LHC.

The parameters of the model can be determined by combining several measurements that can be performed at LHC and at ILC [36]. In general the ability of the LHC to determine the model parameters is limited; however by including the ILC data, associated to the Higgs signals in both visible and invisible final states and also to the $\gamma + \not{E}_T$ signal, a good determination of δ and M_D is possible so long as M_D is not too big [36].

Invisible Higgs decays are discussed further in two contributions in this report: Section 8.2 discusses the weak boson fusion, $Z + h_{inv}$, $t\bar{t} + h_{inv}$ channels at the LHC and describes a new method to extract the Higgs mass from production cross sections. In Section 8.3, the CMS strategy for discovering an invisible Higgs at LHC is presented.

8.1.5 Universal extra dimension and TeV $^{-1}$ models

More general constructions have been proposed, where gravity propagates in the entire 4+δ dimensional space-time, while the SM lives in a subspace with $p \geq 3$ space dimensions. The scale associated to these extra $p-3$ compact dimensions is assumed of the TeV^{-1} size.

The Universal Extra Dimensions model [10] is an extension of the ADD model [1,51] in which all the SM fields, fermions as well as bosons, propagate in the bulk, so that each SM particle has an infinite tower of KK partners. The spin of the KK particles is the same as their SM partners, as well as the strength of the couplings (up to a normalization factor such as $\sqrt{2}$). The minimal UED (mUED) [52,53] scenario is based on the following hypotheses: the fields of the theory propagate in a single extra dimension; the extra dimension is compactified on the orbifold S^1/Z^2 of size R (compactification radius). The choice of the topology is very important since different topologies give different realizations of the low energy theory even when one starts with the same five-dimensional Lagrangian. Compactification on the orbifold has two advantages: only four of the five components of the vector fields and chiral fermions are present in the low energy spectrum. Therefore the SM could be the low energy regime of a UED theory. The tree level Lagrangian has a local five-dimensional Lorentz symmetry responsible for the conservation of the momentum in the extra dimension. The quantum number associated to the symmetry is the KK number. The symmetry, however, is broken due to the presence of additional interactions at the boundaries of the orbifold. But the KK-parity is still conserved with important phenomenological consequences: the lightest massive KK particle (LKP), the KK photon, is stable and can be a candidate for dark matter; the level 1 KK states must be pair produced. 95% CL lower bound on the compactification scale is $M = 1/R \sim 800$ GeV (for a recent analysis, see [11]). Dark matter constraints imply that R$^{-1} \in [600, 1050]$ GeV [13]. The UED Lagrangian in $4+\delta$ dimensions contains two parts, the bulk Lagrangian (SM like) and the boundary interaction terms. If only the bulk Lagrangian is taken into account, the mass of the n-th KK mode is

$$m_n = \sqrt{n^2/R^2 + m_0^2} \tag{8.24}$$

where m_0 is the zero mode mass which could be identified as the SM particles. Therefore the model has a highly degenerate spectrum at each KK level except for large m_0 like t, W, Z, etc. The boundary terms coefficients constitute new free parameters of the model renormalized by the bulk interactions, thus scale dependent. The mUED model assumes they are negligible at the scale $\Lambda > R^{-1}$. In conclusion the mUED has only three parameters R, Λ, m_h. The new terms of this Lagrangian, besides being responsible for breaking the KK number conservation down to the KK parity, split the near degeneracy of each KK level. The corrections to the masses are such that $m_{g_n} > m_{Q_n} > m_{q_n} > m_{W_n} \sim m_{Z_n} > m_{L_n} > m_{l_n} > m_{\gamma_n}$. Therefore the heaviest first level KK modes are pair produced and then cascade decay until the LKP. The experimental signature for KK modes production at hadron colliders will be the missing energy carried away by the LKPs in addition to soft SM leptons and/or jets radiated in the cascade decay

process.

TeV^{-1} models are extra dimension models where electroweak interactions propagate in the bulk, while matter and/or Higgses live on the branes [15, 54, 55]. These models are more constrained than the UED ones, since, due to fact that there is no KK number conservation, KK excitations of gauge bosons can mix with the standard electroweak gauge bosons. Using the electroweak precision measurements, 95% CL lower bound on the compactification scale is $R^{-1} \sim 5 - 6$ TeV [14–21, 56]. A second peculiar consequence is that these KK excitations of W, Z and γ can be singly produced at LHC [57, 58]. The discovery potential of LHC for the heavy neutral resonances using the e^+e^- decay channel will be discussed in detail in 8.4.

8.2 Invisibly decaying Higgs at the LHC

Heather E. Logan

In models of large extra dimensions, the Higgs boson often acquires an invisible decay width. This invisible width, Γ_{inv}, can be due to the mixing of the Higgs with graviscalars which escape the detector [32, 46, 47]. It can also arise from Higgs decays to Kaluza-Klein neutrinos if neutrinos are allowed to propagate in the bulk [59]. In particular, if $m_h < 160$ GeV $\simeq 2\, m_W$ so that the Higgs partial width into SM particles is very small, the invisible width Γ_{inv} can dominate the Higgs width, so that the Higgs decays predominantly into invisible modes. An invisibly decaying Higgs can also arise in supersymmetric models, with Higgs decays to pairs of lightest neutralinos or to a neutralino plus neutrino in models with Higgs-sneutrino mixing due to R-parity violation [60]; in Majoron models [61, 62]; and in generic models of dark matter containing a stable singlet scalar [63–65]. The combined LEP experimental bound on the mass of an invisibly-decaying Higgs boson is 114.4 GeV at 95% confidence level [66], assuming the Higgs is produced with Standard Model rate.

In this contribution we review existing studies [67–75] of detection of an invisibly decaying Higgs boson at the LHC. If the invisible branching fraction is large enough that the usual visible Higgs signals drop below the 5σ threshold, the Higgs mass will be difficult to measure at the LHC; we describe a new method [75] to extract the Higgs mass from production cross sections in a fairly model independent way.

8.2.1 Invisible Higgs detection at LHC

Studies of an invisibly decaying Higgs h_{inv} typically assume Standard Model Higgs production cross sections and a 100% invisible branching fraction. Results can easily be rescaled for non-SM Higgs production rates and partly-visible decay branching fractions. The signal rate is simply scaled by the production rate and invisible branching fraction:

$$S = S_0 \frac{\sigma}{\sigma_{SM}} \frac{\mathrm{BR}_{inv}}{1}, \tag{8.25}$$

where S_0 is the signal rate from the studies, σ/σ_{SM} is the ratio of the nonstandard production cross section to that of the SM Higgs, and BR_{inv} is the invisible branching fraction. Ignoring systematic uncertainties and assuming that the SM is the only source of background, the luminosity required for a given signal significance then scales like

$$\mathcal{L} = \mathcal{L}_0 \left[\frac{\sigma}{\sigma_{SM}} \frac{\mathrm{BR}_{inv}}{1} \right]^{-2}, \tag{8.26}$$

where $\mathcal{L}_0$ is the luminosity required for a given significance found in the studies. Certainly, many models of new physics that can give rise to an invisibly decaying Higgs boson can also give rise to non-SM backgrounds with large missing energy, which must then be dealt with in order to isolate the invisibly-decaying Higgs signal. The studies discussed below assume only SM backgrounds.

Weak boson fusion

Production of an invisible Higgs via weak boson fusion (WBF) was studied for the LHC in Refs. [70,72] and in Section 8.3 of this report. These studies showed that WBF could provide significant signals for invisible Higgs discovery, even at low luminosity. The most important backgrounds are Zjj (with $Z \to \nu\bar{\nu}$) and Wjj (with $W \to \ell\nu$ and the lepton missed), with the jets produced by either QCD or electroweak (EW) processes. The QCD backgrounds are reduced by taking advantage of the colour-flow structure of these backgrounds versus the signal: the two jets in the QCD backgrounds are colour-connected while those in the signal process (and the EW backgrounds) are not. This leads to a depletion of gluon emission in the region between the two jets in the signal process; the QCD background can then be suppressed by vetoing additional soft jet activity in the central region [76]. Applying this central jet veto and characteristic "WBF cuts", the parton-level study in Ref. [70] found a significance of $S/(\sqrt{B} + \Delta B) \simeq 15$ (6.4) for $m_h = 120$ (400) GeV and 10 fb^{-1}. Note that this study takes into account a "systematic" uncertainty ΔB on the background normalization, arising from a separate analysis of the uncertainty on a direct background measurement from data on Zjj (with $Z \to \ell\ell$) and Wjj (with $W \to \ell\nu$ and the lepton detected) events. A 5σ detection of h_{inv} is possible for Higgs masses up to 480 (770) GeV with 10 (100) fb^{-1} [70]. This large Higgs mass reach is characteristic of WBF processes, which proceed through t-channel weak boson exchange and thus fall slowly with increasing Higgs mass.

The analysis was extended with a more realistic experimental simulation in Ref. [72], which considered the importance of triggering on high rapidity jets, as well as the impact of showering and detector effects on the central jet veto, which is not yet well understood. Signal and background cross sections in [72] are generally in good agreement with the parton-level results [70], with the exception of the central jet veto. Analytic calculations [77] of soft central jet production used in [70] lead to a factor 2 smaller QCD Wjj, Zjj backgrounds compared to Pythia generation; taking the more pessimistic Pythia backgrounds leads to a significance of $S/(\sqrt{B} + \Delta B) \simeq 5.6$ (4.7) for $m_h = 120$ (250) GeV and 10 fb^{-1} [72]. For the relatively soft central jets that dominate in the QCD background processes, it is believed that a resummation is needed and the perturbative showering in Pythia is unreliable; this was the purpose of the analytic calculations [77].

$Z + h_{inv}$

Discovery of the Higgs in the $Z + h_{inv}$ channel was studied for the LHC in Refs. [68, 69, 73, 75]. (This channel was also analyzed for the Tevatron in Ref. [78].) The signal is $Z(\to \ell\ell) + h_{inv}$, where $\ell = e, \mu$. The most important backgrounds are $Z(\to \ell\ell)Z(\to \nu\bar{\nu})$, $W(\to \ell\nu)W(\to \ell\nu)$, $Z(\to \ell\ell)W(\to \ell\nu)$ where the lepton from the W decay is missed, $t\bar{t}$ with each top decay yielding a lepton, and $Z(\to \ell\ell) + \text{jets}$ with fake $\not{p}_T$ from jet energy mismeasurements or jets escaping down the beam hole.

The WW background can be largely eliminated by requiring that the $\ell^+\ell^-$ invariant mass is close to the Z mass. This requirement introduces a dependence on the electron and muon energy resolution of the LHC detectors. A cut on the azimuthal angle of the lepton pair eliminating back-to-back leptons also reduces the WW background and eliminates Drell-Yan backgrounds with fake $\not{p}_T$ caused by mismeasurement of the lepton energies. The WZ background is reduced by vetoing events with a third isolated lepton. The $Z + \text{jets}$ background with fake $\not{p}_T$ can be largely eliminated by vetoing events with hard jets; for this the large rapidity coverage of the LHC calorimetry is vital [69]. The jet veto and the cut on the $\ell^+\ell^-$ invariant mass also largely eliminate the $t\bar{t}$ background.

The ZZ background is largely irreducible, but can be controlled to some extent with a cut on $\not{p}_T$. The number of $\ell^+\ell^-\not{p}_T$ signal events typically falls more slowly with $\not{p}_T$ than those of the ZZ or WW backgrounds. The $\not{p}_T$ of the WW background is typically quite low because the $\not{p}_T$ comes from the two neutrinos emitted independently in the two W decays. Although the $\not{p}_T$ of the ZZ background is also typically not quite as large as that of the signal, due to the t-channel nature of the ZZ background in which the Z decaying to neutrinos itself tends to carry less p_T than the h_{inv} produced via s-channel Higgsstrahlung, this background still dominates after cuts. The $\not{p}_T$ distribution of the signal is somewhat sensitive to the Higgs mass; it falls off more slowly with increasing $\not{p}_T$ as m_h gets larger. Thus a fit to

the $\not{p}_T$ distribution can in principle give some (very) limited sensitivity to the Higgs mass.

The parton-level study in Ref. [75] found a significance of $S/\sqrt{B} \simeq 5.3$ (2.9) for $m_h = 120$ (160) GeV and 10 fb^{-1}. This is in good agreement with the results of the more realistic experimental simulation in Ref. [73], which included hadronization of the $Z + h_{inv}$ signal and backgrounds using Pythia/Herwig. For comparable cuts, Ref. [73] found a signal cross section smaller by about 30% and a total background cross section (dominated by ZZ production) smaller by about 20% compared to Ref. [75]; this reduction in both signal and background cross sections is due to events being rejected by the jet veto imposed in Ref. [73] after including QCD initial-state radiation. However, the 30% reduction in signal cross section is compensated [78] by the known NLO QCD K-factor for $Z + h$ at LHC of about 1.3 [79, 80], and the reduction in the dominant ZZ background is compensated by the known NLO QCD K-factor for ZZ at LHC of about 1.2 [81, 82], yielding cross sections consistent with the leading order partonic results [75].

The channel $W + h_{inv}$ was also studied in Refs. [68, 73]; however, in the leptonic W decay channels the signal is $\ell + \not{p}_T$ and is swamped by overwhelming backgrounds.

$\underline{t\bar{t} + h_{inv}}$

Detection of h_{inv} produced by Yukawa radiation off of a top quark pair was studied for the LHC in Refs. [67, 71]. The most important background is $t\bar{t}$ production, with $t\bar{t}Z$, $t\bar{t}W$, $b\bar{b}Z$, and $b\bar{b}W$ also contributing. The analysis in Ref. [71] reconstructs one top quark in its hadronic decay mode and requires an isolated lepton (electron or muon) from the decay of the second top quark along with large missing transverse energy. Both b quarks from the two top decays are required to be tagged.

Ref. [71] found a background after cuts dominated by $t\bar{t}$ production with one top decaying leptonically and the other decaying to a tau. Vetoing the taus would significantly improve the results but was beyond the scope of the study in [71]. From the results of Ref. [71] we calculate a significance of $S/\sqrt{B} \simeq 2.0$ (0.7) for $m_h = 120$ (200) GeV and 10 fb^{-1}. If the background from top decays to taus could be eliminated, this would improve to $S/\sqrt{B} \simeq 3.2$ (1.1) for $m_h = 120$ (200) GeV. The signal observability should not degrade significantly for the high-luminosity LHC running; thus the $S/\sqrt{B}$ numbers quoted can be scaled up by $\sqrt{30}$ to estimate the ultimate LHC sensitivity with 300 fb^{-1}: i.e., $S/\sqrt{B} \simeq 11.1$ (3.8) [17.7 (6.0)] for $m_h = 120$ (200) GeV including [excluding] the $t \to \tau$ background. More experimental work is needed to understand the systematic uncertainties in both physics and detector simulation.

Although the discovery potential of this mode is much less than that of WBF or $Z + h_{inv}$, its study is well motivated because it offers access to the coupling of h_{inv} to top quarks. This may well be the only Higgs coupling to SM fermions measurable at the LHC in the case that BR$(h \to \text{invisible}) \sim 100\%$, and thus provides a valuable input to the study of electroweak symmetry breaking.

Diffraction

Detection of h_{inv} produced by central exclusive diffraction at the LHC was studied in Ref. [74]. The signal process is $pp \to ph_{inv}p$, with the two final-state protons very forward. In such a process, the mass of the Higgs boson can be very accurately measured using the missing-mass method; the sharp peak in the missing mass spectrum dramatically reduces background contributions. In fact, one can imagine using an ILC-style missing-mass analysis to measure the $pp \to php$ cross section and h branching fractions in a model-independent way. Further, such a "Pomeron-Pomeron fusion" process can only produce neutral, colourless, flavourless particles of parity $P = (-1)^J$, enabling these quantum numbers of the invisibly decaying state to be pinned down.

The difficulty arises in detecting and triggering on $ph_{inv}p$ events. The final-state protons must be detected by far-forward proton detectors (roman pots or microstations) installed up to 400 m from the interaction point. These detectors would register protons that have lost a small fraction of their incoming energy through the diffractive process; the trigger would have to be on the far-forward protons, since h_{inv} leaves "nothing" (except noise) in the central detector. The main backgrounds consist of soft inelastic Pomeron-Pomeron fusion yielding hadrons in the central detector and events in which the

Table 8.2: Higgs mass determination from $Z + h_{inv}$ with 10 (100) fb^{-1}, assuming Standard Model production cross section and 100% invisible decays. The signal and background cross sections were taken from Table I of Ref. [75] for the cut $\not{p}_T > 75$ GeV. The total uncertainty includes a theoretical uncertainty on the signal cross section from QCD and PDF uncertainties of 7% [83] and an estimated lepton reconstruction efficiency uncertainty of 4% (2% per lepton) and luminosity normalization uncertainty of 5% [84]. From Ref. [75].

m_h (GeV)	120	140	160
$\rho = (d\sigma_S/dm_h)/\sigma_S$ (1/GeV)	-0.013	-0.015	-0.017
Statistical uncert.	21% (6.6%)	28% (8.8%)	37% (12%)
Background normalization uncert.	33% (10%)	45% (14%)	60% (19%)
Total uncert.	40% (16%)	53% (19%)	71% (24%)
Δm_h (GeV)	30 (12)	35 (12)	41 (14)

final-state protons lose energy through QED radiation. In order for the Higgs events to be separated, these backgrounds must be suppressed by forward calorimeters able to reject events with additional high-energy photons and charged pions with very high efficiency [74].

8.2.2 Higgs boson mass measurement

The mass of an invisibly-decaying Higgs boson obviously cannot be reconstructed from the Higgs decay products. Unless the Higgs is also observed in a visible channel, our only chance of determining the Higgs mass at the LHC comes from the m_h dependence of the production process. Here we describe the method of Ref. [75] to extract the Higgs boson mass from cross sections in a fairly model-independent way.

Extracting m_h from the cross section of a single production channel requires the assumption that the production couplings are the same as in the SM. Non-observation of the Higgs in any visible final state implies that the invisible branching fraction is close to 100%. The Higgs mass extraction from LHC measurements of the production cross sections in $Z + h_{inv}$ and WBF under these assumptions are shown in Tables 8.2 and 8.3, respectively. There are two main sources of uncertainty in the signal: statistical and from background normalization. The statistical uncertainty is $\Delta\sigma_S/\sigma_S = \sqrt{\mathrm{S}+\mathrm{B}}/\mathrm{S}$. Ref. [75] estimated the total background normalization uncertainty for $Z + h_{inv}$ to be the same size as that of the dominant process involving $Z \to \nu\bar{\nu}$: $\Delta\mathrm{B}/\mathrm{B} = \Delta\mathrm{B}(ZZ)/\mathrm{B}(ZZ)$. They assumed that this background can be measured via the corresponding channels in which $Z \to \ell^+\ell^-$ and took the uncertainty to be the statistical uncertainty on the $Z \to \ell^+\ell^-$ rate: $\Delta\mathrm{B}(ZZ)/\mathrm{B}(ZZ) \simeq 7.1\%$ (2.2%), for an integrated luminosity of 10 (100) fb^{-1}. Tables 8.2 and 8.3 quote the resulting uncertainty on the signal cross section, given by $\Delta\sigma_S/\sigma_S = (\mathrm{B}/\mathrm{S}) \times \Delta\mathrm{B}/\mathrm{B}$. The total uncertainty $[\Delta\sigma_S/\sigma_S]_{tot}$ presented in Tables 8.2 and 8.3 is then the sum, in quadrature, of the statistical and background uncertainties, as well as the other uncertainties described in the table captions. We then have $\Delta m_h = (1/\rho)[\Delta\sigma_S/\sigma_S]_{tot}$, where $\rho \equiv (d\sigma_S/dm_h)/\sigma_S$ is the "slope" of the cross section.

The cross section for $Z + h_{inv}$ production falls quickly with increasing m_h due to the s-channel propagator suppression. This is in contrast to the WBF production, which provides a $> 5\sigma$ signal up to $m_h \simeq 480$ GeV with 10 fb^{-1} if the Higgs decays completely invisibly [70]. Thus, while the statistics are much better on the WBF measurement than on $Z + h_{inv}$, the systematic uncertainties hurt WBF more because $(d\sigma_S/dm_h)/\sigma_S$ is much smaller for WBF than for $Z + h_{inv}$. The $Z + h_{inv}$ cross section is therefore more sensitive to the Higgs mass than the WBF cross section.

More importantly, however, taking the ratio of the $Z + h_{inv}$ and WBF cross sections allows for a more model-independent determination of the Higgs mass. This is due to the fact that the production couplings in $Z + h_{inv}$ (hZZ) and in WBF (contributions from hWW and hZZ) are related by custodial

Table 8.3: Higgs mass determination from WBF $\to h_{inv}$ with 10 (100) fb^{-1}, assuming Standard Model production cross section and 100% invisible decays. The background and signal cross sections were taken from Tables II and III, respectively, of Ref. [70], and include a central jet veto. The total uncertainty includes a theoretical uncertainty from QCD and PDF uncertainties of 4% [85, 86], and an estimated uncertainty on the efficiency of the WBF jet tag and central jet veto of 5% and luminosity normalization uncertainty of 5% [84]. From Ref. [75].

m_h (GeV)	120	130	150	200
$\rho = (d\sigma_S/dm_h)/\sigma_S$ (1/GeV)	-0.0026	-0.0026	-0.0028	-0.0029
Statistical uncert.	5.3% (1.7%)	5.4% (1.7%)	5.7% (1.8%)	6.4% (2.0%)
Background normalization uncert.	5.2% (2.1%)	5.3% (2.1%)	5.6% (2.2%)	6.5% (2.6%)
Total uncert.	11% (8.6%)	11% (8.6%)	11% (8.6%)	12% (8.8%)
Δm_h (GeV)	42 (32)	42 (33)	41 (31)	42 (30)

Table 8.4: Higgs mass determination from the ratio method discussed in the text, with 10 (100) fb^{-1}. The event rates for WBF were interpolated linearly for Higgs masses of 140 and 160 GeV, which were not given explicitly in Ref. [70]. Statistical uncertainties were obtained assuming SM signal rates. The total uncertainty includes theoretical uncertainties from QCD and PDF uncertainties of 7% for $Z + h_{inv}$ [83] and 4% for WBF [85, 86], and estimated uncertainties on the lepton reconstruction efficiency in $Z + h_{inv}$ of 4% (2% per lepton) and on the efficiency of the WBF jet tag and central jet veto of 5% [84]. The luminosity normalization uncertainty cancels out in the ratio of cross sections and is therefore not included. From Ref. [75].

m_h (GeV)	120	140	160
$r = \sigma_S(Zh)/\sigma_S(\mathrm{WBF})$	0.132	0.102	0.0807
$(dr/dm_h)/r$ (1/GeV)	-0.011	-0.013	-0.013
Total uncert., $\Delta r/r$	41% (16%)	54% (20%)	72% (25%)
Δm_h (GeV)	36 (14)	43 (16)	53 (18)

SU(2) symmetry in any model containing only Higgs doublets and/or singlets. The production couplings thus drop out of the ratio of rates in this wide class of models (which includes the MSSM, multi-Higgs-doublet models, and models of singlet scalar dark matter), leaving dependence only on the Higgs mass. (The dependence on the invisible branching fraction of the Higgs also cancels in the ratio.) The resulting Higgs mass extraction is illustrated in Table 8.4. Assuming SM event rates for the statistical uncertainties, the Higgs mass can be extracted with an uncertainty of $\pm$35–50 GeV ($\pm$15–20 GeV) with 10 (100) fb^{-1} of integrated luminosity. The ratio method also allows a test of the SM cross section assumption by checking the consistency of the separate m_h determination from the $Z + h_{inv}$ or WBF cross section alone with the m_h value extracted from the ratio method. Furthermore, observation of the invisibly-decaying Higgs in WBF but not in $Z + h_{inv}$ allows one to set a lower limit on m_h in this class of models.

8.3 Search for invisible Higgs decays in CMS

Kajari Mazumdar and Alexandre Nikitenko

There are several scenarios beyond Standard Model where the Higgs boson can decay invisibly [87]. These mechanisms also modify the production and decay rates of the Higgs in visible modes at the LHC and hence model-independent, experimental investigation for invisible decay of Higgs boson constitutes an essential aspect of the Higgs search program at the collider experiments..

The discovery potential of an invisible Higgs boson in the context of the LHC has been discussed in various production modes. The sensitivities of the CMS detector for the invisibly decaying Higgs boson, when it is produced via vector boson fusion (VBF) process [70], have been evaluated in [88] with CMS-specific detailed detector simulation and event reconstruction softwares. We discuss here the salient features.

8.3.1 Invisible Higgs boson signal and the background

We note that in the invisible decay channel no mass can be reconstructed and hence the discovery is established by observing an excess of events compared to predicted backgrounds. Therefore sufficient signal cross-section and a good signal-to-background ratio are the requirements for the experimental search. In gluon-gluon fusion process the final state is *nothing* and hence can't even be identified. The VBF channel offers the highest cross-section among all the processes where Higgs is not produced alone in the final state and thus provides a handle to tag the event via accompanying particle(s).

The dynamics of the signal channel in the VBF process leads to energetic jets in the forward and backward directions due to the continuation of the interacting quarks in original direction, after the simultaneous emission of W/Z bosons. The absence of colour exchange between the scattered quarks and the colourless Higgs boson leads to low hadronic activity in the central region. Consequently, this process has special signature of two jets with distinct topology in the final state: (i) the rapidity gap between the jets is large, (ii) the jets are in opposite hemispheres, (iii) the jets carry large energy and so invariant mass of jets is large.

There are several SM processes which can have similar final state as this signal. For the final state under study, *ie,* 2 jets plus missing energy, QCD di-jet production may mimic the signal characteristics, the rate being very high. The other SM processes, QCD and electroweak production of W + 2jets and Z + 2jets events with leptonic decays of the W, Z bosons which, in particular, are potential backgrounds. For $W \to \ell\nu$ and $Z \to \ell\ell$ events with $(\ell = e, \mu, \tau)$ and e, μ decays of τ, if the charged lepton is not identified within the detector acceptance, the final state effectively consists of 2 jets and missing energy. The genuine background is due to the process $Z \to \nu\bar{\nu}$ and the event is almost similar to the signal when Z + 2 jets events are produced via weak interaction (t-channel exchange of W). As will be discussed later, fortunately the jets in the signal channel seem to balance the Higgs and hence the angle between the jets is smaller which is not the case for these background events when the satisfy VBF like criteria.

The search strategy heavily relies on the optimal performance of the calorimeters of the LHC detectors for jets and missing transverse energy ($E_T^{\rm miss}$) reconstruction as well as on a dedicated calorimeter trigger.

8.3.2 Event generation, simulation and reconstruction

The signal events, $qq \to qqH,\ H \to invisible$ were generated with PYTHIA event generator, [89], and using the CTEQ5L structure function parameterization. Since the process $H \to invisible$ is not actually available in PYTHIA, we generated $H \to ZZ(^*) \to \nu\bar{\nu}\nu\bar{\nu}$. We produced signal samples for different Higgs masses ranging from $110 - 400$ GeV. The SM production cross section considered is calculated by the VV2H program [90]. The PYTHIA package was also used to simulate QCD di-jet production (MSEL=1) processes, in various $\hat{p_T}$ bins from $10 - 15$ GeV ($\sigma = 8.868 \times 10^{12}$ fb) up to 2600-3000 GeV ($\sigma = 11.25$ fb) for a total of about 10^6 events.

For W + 2jets and Z + 2jets processes ($2 \to 3$) parton level events were produced, according to Leading Order matrix element calculations, with dedicated event generators combined with forced leptonic decays. The QCD subprocess events were produced with MadCUP [91] based on the work of [92] using CTEQ4L structure function. The electroweak subprocess events were generated with the COMPHEP generator [93], with the CTEQ5L structure function. The parton level events were subsequently hadronized through PYTHIA. The production rates were found to be in good agreement with the values

Table 8.5: Cross sections (in pb) for backgrounds as given by LO matrix element calculations with preselection cuts described in the text. $\mathrm{BR}(Z \to \nu\nu)$ and $\mathrm{BR}(W \to \ell\nu)$ are included.

QCD Wjj	QCD Zjj	EW Wjj	EW Zjj
76.0	15.7	4.7	0.644

Table 8.6: Survival probabilities for signal and background for a veto on central jets with $E_T > 20$ GeV [77].

Signal	QCD W + 2jets & QCD Z + 2jets	EW W + 2jets & EW Z + 2jets
0.87	0.28	0.82

from other packages, Madgraph [94] and ALPGEN [95].

Loose selection criteria were used to generate W + 2jets and Z + 2jets events.

$$p_T^{1,2} > 20 \text{ GeV}, \;\; |\eta_{1,2}| < 5.0, \;\; |\eta_1 - \eta_2| > 4.2, \;\; \eta_1 \times \eta_2 < 0, \;\; M_{1,2} > 900 \text{ GeV}$$

where 1 and 2 refer to the partons (gluons and quarks) accompanying Z and W production. The cross sections (in pb) given by the matrix element calculations with these cuts are presented in Table 8.5. Cross sections include the leptonic branching ratios, $\mathrm{BR}(Z \to \nu\bar{\nu})$ and $\mathrm{BR}(W \to \ell\nu)$, for three lepton generations.

All the signal samples and QCD multijet events after generation are fully simulated in CMS detector, using GEANT-based detector simulation package CMSIM [96]. Subsequently the events were digitized and reconstructed with CMS-specific reconstruction software ORCA [97]. Event pile up, corresponding to instantaneous luminosity of $2{\times}10^{33}$ cm^{-2} s^{-1}, was taken into account. The W + 2jets and Z + 2jets events were processed using the fast simulation package CMSJET [98].

A key point of the search is the use of a mini-jet veto, namely the rejection of events with additional soft ($E_T > 20$ GeV) jet(s) inside the rapidity gap between the two forward tagging jets as discussed before. The efficiency of the mini-jet veto is expected to be sensitive to detector effects like calibration, electronic noise and readout thresholds, interaction of soft particles in the tracker in front of the calorimeter, magnetic field, or pile up activity. Since the fast CMSJET simulation is not expected to properly reproduce these effects, the mini-jet veto efficiency was not evaluated for the background events with CMSJET. Instead the background efficiency was multiplied by P_{surv}, defined as the probability for a jet (parton) to be radiated in the rapidity gap between the two tagging jets and with the $\mathrm{E_T} > 20$ GeV cut. The values of P_{surv} calculated in [77] and used in the analysis [70] are listed in Table 8.6. In the parton level study it has been assumed that such jets will be reconstructed with 100 % efficiency. The effect of the central jet veto is realistically evaluated for the Higgs boson signal with detailed simulations and it causes a 24 % reduction of the signal which is worse than that quoted in [70].

8.3.2.1 Event Analysis

For the present analysis the signal-to-background ratio is effectively enhanced by identifying the forward jets obeying topological features and applying further requirements on the effective mass of the tagging jets (M_{jj}), the missing transverse energy (E_T^{miss}) and the azimuthal angle between the two jets in the transverse plane (ϕ_{jj}). These are

$$E_T^{\mathrm{j1,\,j2}} > 40 \text{ GeV}, \;\; |\eta_{\mathrm{j1,\,j2}}| < 5.0, \;\; |\eta_{\mathrm{j1}} - \eta_{\mathrm{j2}}| > 4.4, \;\; \eta_{\mathrm{j1}} \times \eta_{\mathrm{j2}} < 0, \tag{8.27}$$

$$E_T^{\mathrm{miss}} > 100 \text{ GeV} \tag{8.28}$$

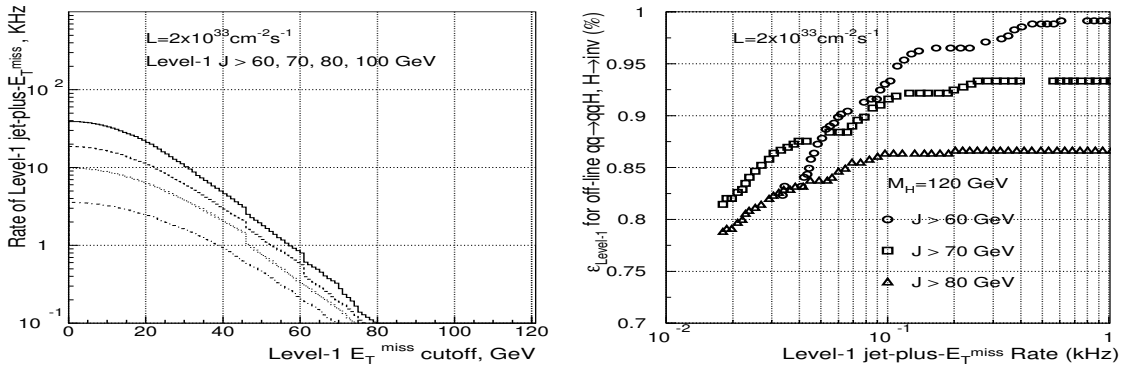

Fig. 8.6: Rate of L1 jet−plus−$E_T^{\rm miss}$ trigger as a function of $E_T^{\rm miss}$ threshold for given values of jet threshold. Trigger rate vs efficiency for $qq \to qqH,\ H \to invisible$ events which passed VBF cuts.

$$M_{\rm jj} \ > \ 1200 \ {\rm GeV}, \tag{8.29}$$

$$\phi_{\rm jj} \ < \ 1 \ {\rm rad} \tag{8.30}$$

In addition a mini-jet veto in the central region, and a lepton veto, i.e. the requirement that no lepton be reconstructed with transverse momentum $p_T > p_T^{\rm cut}$, $p_T^{\rm cut}$ = 10 (5) GeV for electron (muon) have also been used. In the present study the veto on taus is separated into a lepton veto and a jet veto, depending on whether the tau decays leptonically or hadronically. The full set of these cuts we shall refer to, hereafter, as VBF cuts.

8.3.2.2 Triggers

At LHC the collision and the overall data rate being much higher than the data archival storage capability the required rejection power, $\mathcal{O}(10^5)$, is achieved in two steps for CMS experiment. At lower level (L1) the trigger conditions are implemented through hardware and in the second/higher level (HLT) selection algorithms are executed in processor farm [99]. The invisible Higgs decay channel requires dedicated calorimeter trigger both at L1 and at HLT. The Hadron Forward calorimeter (HF) of the CMS detector plays a crucial role in the on-line and off-line selections. The combined jet−plus−$E_T^{\rm miss}$ trigger condition is the most effective for the invisible Higgs boson selection. The trigger bandwidth is dominated by QCD jet events which has huge cross-section. At low luminosity, the trigger threshold optimization was performed by studying the trigger rate for jet−plus−$E_T^{\rm miss}$ trigger vs. the signal efficiency by varying the $E_T^{\rm miss}$ threshold for a fixed set of single jet threshold values as illustrated in Fig.8.6. The optimum values were found to be 60 and 64 GeV, corresponding to a signal efficiency of 98%. In the off-line reconstruction both jet E_T and $E_T^{\rm miss}$ are corrected for the effects of calorimeter non-linearity. Jet energy corrections are also applied at L1, while it is not foreseen to correct $E_T^{\rm miss}$ at L1.

At HLT, the off-line requirement (1) on the pseudorapidity gap between the two highest E_T jets can be exploited concurrently with the minimum threshold requirements on $E_T^{\rm miss}$ and $M_{\rm jj}$. Full-granularity calorimeter information is available at HLT and hence jet and $E_T^{\rm miss}$ will be reconstructed like in the off-line analysis. The left plot in Figure 8.7 shows the rate of QCD multi-jet events after cut (1) as a function of the cutoff on $E_T^{\rm miss}$.

8.3.2.3 Event selection

One of the crucial problems of this study is a proper simulation of the tails in the $E_T^{\rm miss}$ distribution of the QCD multi-jet background events which could be due to real $E_T^{\rm miss}$ from heavy quarks decays, but also due to a number of detector effects. To make reliable estimates, a total of about one million of QCD multi-jet events was used. However, this statistics was still not enough to directly prove that the QCD

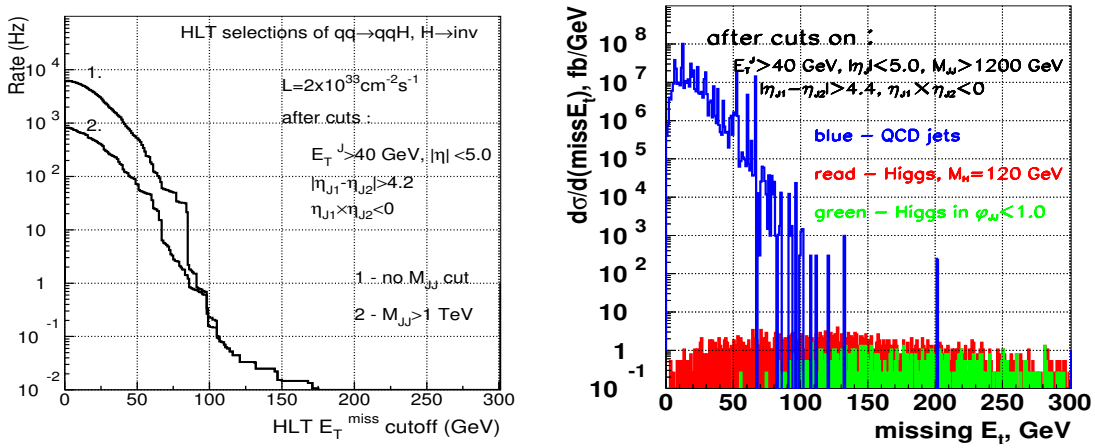

Fig. 8.7: Left:QCD di-jet background rate after jet topological selection (1) as a function of the threshold on $E_T^{\rm miss}$. Right: $E_T^{\rm miss}$ distribution for 120 GeV Higgs boson events (dark shaded area) and for the QCD multi-jet background (open histogram) after selections (1) and (3). $E_T^{\rm miss}$ distribution in signal events after cut (4) is shown as the light shaded area.

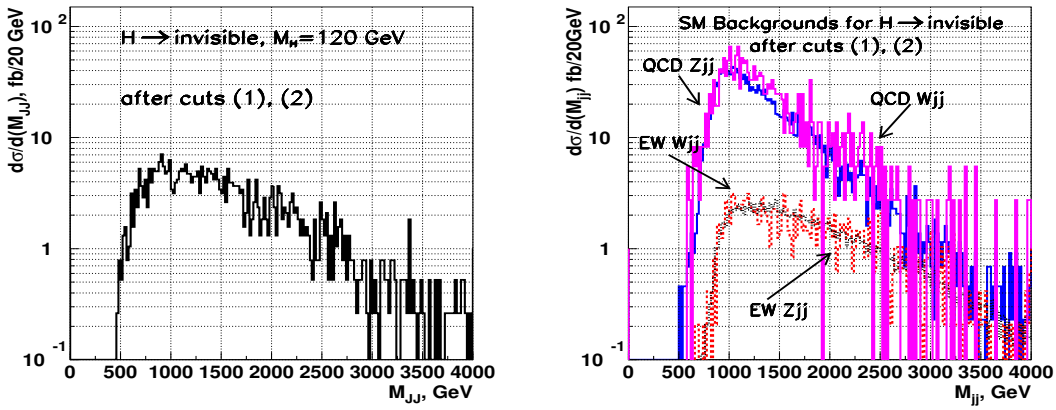

Fig. 8.8: The $M_{\rm jj}$ distribution for 120 GeV Higgs boson and background events after cuts (1-2).

background could be suppressed. The right plot of Figure 8.7 shows the $E_T^{\rm miss}$ distribution of the QCD jet background (open histogram) and of the Higgs boson signal (dark shaded area) after cuts (1) and (3). With an additional cut (4), the $E_T^{\rm miss}$ distribution for the signal events is superposed as the light shaded area. It can be observed that the tail in the background distribution goes well beyond 100 GeV. The QCD multi-jet events in the tail come from $\hat{p_T}$ bins between 300 and 600 GeV. Once the cut (4) on $\phi_{\rm jj}$ is applied, no background event with $E_T^{\rm miss} > 100$ GeV is left. With the statistics used in the analysis, this leads to an upper limit of $\simeq 1$ pb on the QCD background contribution, i.e., about of 10 times higher than the signal expected after the same selections (1-4). In the final analysis for signal observability in CMS, it is assumed that QCD multi-jet events can be entirely suppressed with a cut on the minimal angle in the transverse plane between missing p_T and a jet as implemented in the ATLAS fast simulation study [100]. The $E_T^{\rm miss}$ requirement reduces the W/Z + 2jets backgrounds as well. Figure 8.8 shows the M_{jj} distributions for the signal and background events after cuts (1) and (2) and the same electron, muon veto. In signal events the transverse momenta of the tagging jets balance the $E_T^{\rm miss}$ due to the invisible Higgs boson. An upper threshold on the azimuthal angle between the two jets reduce further the background of W/Z+2 jets types of events as shown in Figure 8.9.

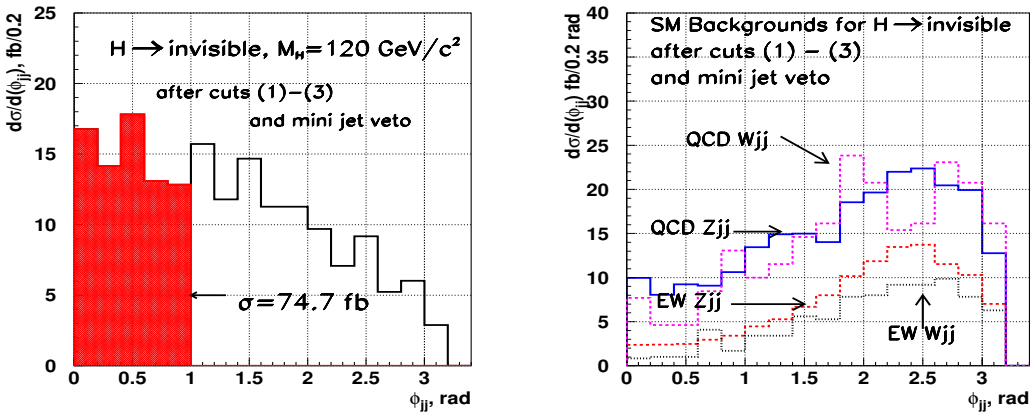

Fig. 8.9: The $\phi_{\rm jj}$ distribution for 120 GeV Higgs boson and background events after cuts (1-3) and mini-jet veto.

Table 8.7: Cross sections in fb for the background and a 120 GeV Higgs boson assuming $\mathrm{BR}(H \to inv.) = 100\%$ and Standard Model production cross section for the Higgs boson.

cross section, fb	Higgs	QCD $Z+2$ jets	QCD $W+2$ jets	EW $Z+2$ jets	EW $W+2$ jets
after cuts (1-3), e,μ veto	238	857	1165	141.5	145.1
+ mini-jet veto	180	240	237	116	84.5
+ $\phi_{\rm jj} \leq 1$ rad.	74.7	48.0	40.0	12.8	8.7

8.3.3 Results

Estimated cross sections (in fb) for the Higgs boson and various types of backgrounds at different steps of the event selection are shown in Table 8.7. SM production cross sections and $\mathrm{BR}(H \to inv.) = 100$ % are assumed. The first row of Table 8.7 presents the cross sections after cuts (1-3) and a veto on identified leptons. The second row presents the cross sections after the mini-jet veto where the survival efficiencies are obtained from Table 8.6. The last row of the Table 8.7 shows the cross sections after all selection cuts.

8.3.4 Limit on branching ratio for invisible decay

It is evident that background estimation is a crucial aspect of this study. At present we have considered the rates of the background events as calculated at the Leading Order. It is expected that at the LHC we can estimate the cross-sections directly from data utilizing W + 2jets and Z + 2jets events for leptonic decays of W, Z where the lepton is identified (and isolated). As estimated in [70], this method leads to a systematic uncertainty on the background evaluation to be about of $\sim 3\%$. It is taken into account along with the statistical uncertainty. The total error on the background cross section is evaluated to be 4.7 fb.

The sensitivity to invisible decay mode of the Higgs boson is defined as 1.96 standard deviation (95 % CL) from the expected background. The absence of a signal can be interpreted as an upper limit on branching ratio for invisible decay of the Higgs boson which can be probed at a given luminosity, assuming SM-like production rate. We define the parameter,

$$\xi = \mathrm{BR}(H \to invisible)\frac{\sigma(qq \to qqH)}{\sigma(qq \to qqH)_{SM}} \tag{8.31}$$

which can be probed at 95% CL as a function of Higgs mass with an integrated luminosity of 10 fb^{-1} as displayed in Figure 8.10.

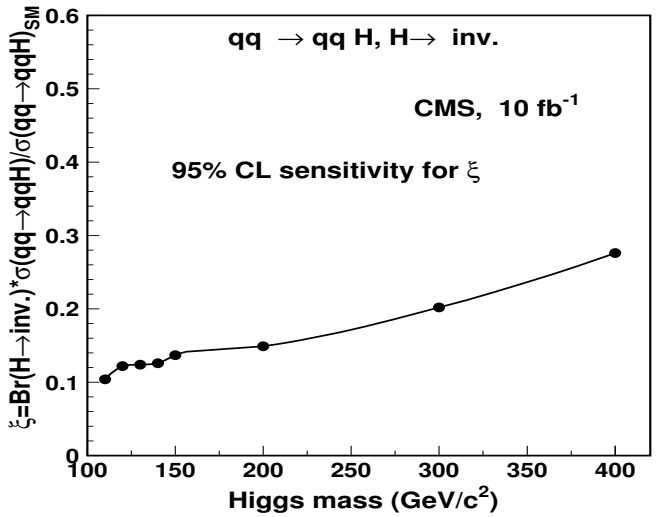

Fig. 8.10: Upper limit of parameter ξ as a function of Higgs boson mass.

8.3.5 Summary

The potential of the CMS experiment for the observability of the Higgs boson in Vector Boson Fusion production channel with an invisible decay has been studied. The viability of the basic selection criteria is checked with realistic detector simulation. The signal channel has very high efficiency for the CMS trigger condition. A reasonably low value for the lower limit on the branching fraction for the invisible mode of the Higgs boson can be obtained with a limited luminosity for a light Higgs boson, for example about 12% for a Higgs mass of 120 GeV.

8.4 Search for heavy resonances

Barbara Clerbaux, Tariq Mahmoud, Caroline Collard, Philippe Miné

As explained in Section 8.1, in addition to large extra dimensions where only gravity may propagate, the electroweak interactions could possibly also propagate in TeV^{-1}-sized extra dimensions. This possibility allows for new model building, which address gauge coupling unification [101] or fermion mass hierarchy [9]. The phenomenological consequence of this scenario is the appearance of a KK tower of states for gauge boson fields. The masses of the gauge boson modes are given by: $M_n^2 = M_0^2 + n^2 M^2$, where M_0 is the mass of the zeroth mode, corresponding to the SM fields, n is the mode number and M is the compactification scale, $M = 1/R$ (R being the compactification radius). In this approach, the existence of only one extra dimension, of radius $R \simeq \mathrm{TeV}^{-1} \simeq 10^{-17}\mathrm{cm}$, compactified on a circle with an orbifold condition, (compactification on S^1/Z^2), is assumed. In the model considered here, all the SM fermions are localized at the same orbifold point. The couplings of fermions to KK gauge bosons are the same as in the SM, but scaled by a factor $\sqrt{2}$. The model has only one free parameter, the compactification scale M.

In fact, heavy resonances with mass above 1 TeV are predicted by several models beyond the Standard Model. Superstring-inspired E_6 models [102] or left-right symmetry-breaking models [103, 104], predict the existence of an extra heavy neutral gauge boson, generically called Z' (c.f. Section 6). Currents lower limits on the Z' mass are (depending on the model) of the order of 600-900 GeV [105]. In addition to the KK Z resonances, we consider six cases of Z' bosons which are frequently discussed and whose properties are thought to be representative of a broad class of extra gauge bosons:

– Z_{SSM} within the Sequential Standard Model (SSM), which has the same couplings as the Standard

Model Z and is often used as a benchmark by experimentalists.

- Z_ψ, Z_η, and Z_χ, arising in E_6 and SO(10) GUT groups.
- Z_{LRM} and Z_{ALRM}, arising in the framework of the so-called "left-right" and "alternative left-right" models. Their couplings were calculated according to the formalism in Ref. [103, 104] with $g_R = g_L$.

In the framework of the Randall and Sundrum (RS) model, see Section 9 of this report, gravitons appear as massive resonances, with masses of order of TeV. Two parameters control the properties of the RS model: the mass of the first KK graviton excitation, and the coupling constant c determining graviton couplings and widths.

In this contribution we present the CMS experiment discovery potential for new heavy resonances, decaying into an electron pair. The e^+e^- decay channel provides a clean signature in the CMS detector. The presence of a heavy particle would be detected in CMS by the observation of a resonance peak in the dielectron mass spectrum over the Drell-Yan process ($pp \to \gamma/Z \to e^+e^-$) which constitutes the main Standard Model background. We also show how to contrast Standard Model Drell-Yan process and Z' production (spin 1) from graviton production (spin 2). Details of the analyses presented in this Section can be found in [106] and [107].

8.4.1 Event selection and correction

Two electrons are requested for this analysis. They are reconstructed as super-clusters (SC) in the CMS electromagnetic calorimeter ECAL in the barrel and the endcap regions [108]. For endcap SC, the energy loss in the preshower detector is taken into account. The two SC with highest energies are selected as the electron candidates.

An important characteristic of the signal events is that the final state electrons are very energetic and may have a significant energy leakage beyond the ECAL clusters. An improvement in the energy determination is achieved by including the hadronic calorimeter HCAL measurement, event by event.

Reducible backgrounds (like QCD jets and γ-jets) are suppressed by applying the following requirements:

- The ratio of the HCAL to ECAL energy deposits is required to be $H/E < 10\%$.
- The two SC must be isolated: the total additional transverse energy in a cone of radius $0.1 < \Delta R < 0.5$ is required to be below 2% of the SC transverse energy (where $\Delta R = \sqrt{\Delta\eta^2 + \Delta\phi^2}$).
- To identify electrons and reject neutral particles, a track is requested to be associated for each electron candidate. If a track is associated with only one of these SC, the event is however kept if it contains a third SC with $E > 300$ GeV with an associated track and satisfying the H/E and isolation cuts described above.

The selected events are then corrected for the following effects:

- Saturation correction: for very energetic electrons and photons, saturation occurs in the ECAL electronics because of the limited dynamical range of the Multi-Gain-Pre-Amplifier. The saturation threshold has been established to be at 1.7 TeV in crystals of the barrel and 3.0 TeV in the endcaps. A correction method (for barrel only) has been developed using the energy deposit in crystals surrounding the saturated crystal. The correction leads to the correct estimate of energy deposit with a resolution of around 7% [109].
- Energy correction: the ECAL measured electron energy after preshower, HCAL and saturation corrections, is smaller than the generated energy. Dedicated energy correction factors for very energetic electrons have been determined using calibration files. These factors depend on both energy, η and whether saturation occurs or not. The resolution on the corrected SC energy is 0.6% at $E = 1000$ GeV.
- z-vertex distribution: the measurement in η takes into account the knowledge of the z-vertex position.

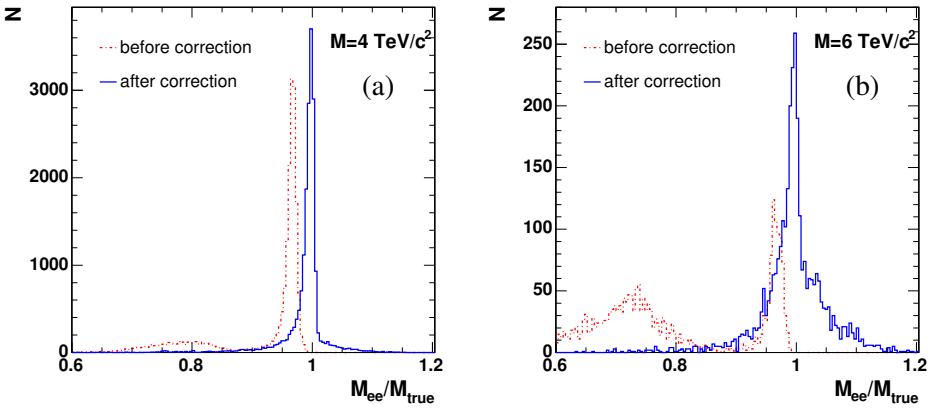

Fig. 8.11: Ratio $M_{\rm ee}/M_{\rm true}$ before and after corrections for KK Z boson production, for $M = 4$ TeV (a) and $M = 6$ TeV (b).

– FSR recovery: hard photon emission from Final State Radiation can induce the detection in the event of a third energetic SC. If a SC with $E > 300$ GeV satisfying the H/E and isolation cuts is observed very close to the SC of the electron candidates ($\Delta R < 0.1$), this additional SC is associated to the corresponding electron.

The signal efficiency for the three heavy resonance production models is typically of the order of 80%.

8.4.2 Mass peak distributions

The resonance mass is reconstructed from the energies and angles of the 2 electron candidates, after the selection cuts and energy corrections mentioned above. Figures 8.11(a) and (b) show the ratio of the reconstructed and the true masses, $M_{\rm ee}/M_{\rm true}$, before and after energy corrections for KK Z production with M =4 and 6 TeV, respectively. The peaks at low values of $M_{\rm ee}/M_{\rm true}$ correspond to events with saturated ECAL electronics. The final resolution on the resonance mass is around 0.6% for events with no saturation, and 7% in case of saturation.

Figure 8.12(a) presents the signal and the Drell-Yan background for KK Z boson production with $M = 4$ TeV; Figure 8.12(b) for Z' boson production with $M = 3.0$ TeV; Figure 8.12(c) for graviton production with $M = 1.5$ TeV and coupling parameter $c = 0.01$.

8.4.3 Discovery potential of CMS

The discovery potential of a new physics resonance is determined using the likelihood estimator S based on event counting [110], suited for small event samples:

$$S = \sqrt{2[(N_{\rm s} + N_{\rm b})\log(1 + \frac{N_{\rm s}}{N_{\rm b}}) - N_{\rm s}]}, \tag{8.32}$$

where $N_{\rm s}$ (resp. $N_{\rm b}$) is the number of signal (resp. background) events. The discovery limit is defined by $S > 5$.

The number of signal and background events, $N_{\rm s}$ and $N_{\rm b}$, computed for a given mass window around the peak, are presented in Table 8.8 for the three models, together with the corresponding significance, for an integrated luminosity of 30 fb^{-1}. The 5σ discovery limits as a function of mass are given in

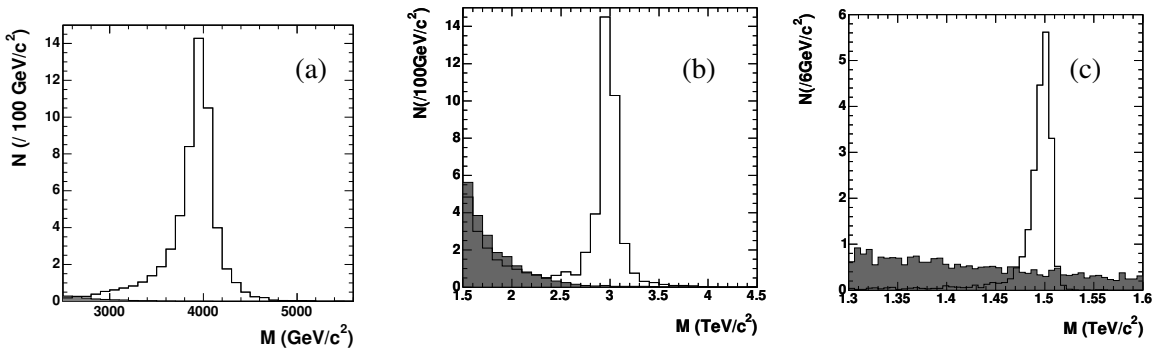

Fig. 8.12: Resonance signal (white histograms) and Drell-Yan background (shaded histograms) for KK Z boson production with $M = 4.0$ TeV (a), SSM Z' boson production with $M = 3.0$ TeV (b), and graviton production with $M = 1.5$ TeV, $c = 0.01$ (c), for an integrated luminosity of 30 fb^{-1}.

Fig. 8.13(a) and Fig. 8.13(b), for KK Z boson production and Z' production (for the 6 considered models), respectively. In the graviton case, the 5σ discovery plane as a function of the coupling parameter c and the resonance mass is given in Fig. 8.13(c).

For KK Z bosons, a 5σ discovery can be achieved for a resonance mass up to $M = 4.97$ TeV for an integrated luminosity of 10 fb^{-1}, $M = 5.53$ TeV for 30 fb^{-1} and $M = 5.88$ TeV for 60 fb^{-1}.

For Z' boson production, with an integrated luminosity of 30 fb^{-1}, a 5σ discovery can be extracted for masses up to 3.31 TeV for model ψ and up to 4.27 TeV for model ARLM.

For gravitons, with an integrated luminosity of 30 fb^{-1}, a 5σ discovery can be extracted for masses up to 1.64 TeV for $c = 0.01$ and up to 3.81 TeV for $c = 0.1$. Similar discovery limits are obtained in the graviton di-photon decay channel (see Section 9.5).

The 5σ discovery limits on the resonance masses for 10, 30 and 60 fb^{-1} are summarized in Table 8.9.

For KK Z boson production, the luminosities needed for a 5σ discovery are 1.5, 4.0, 10.8, 29.4, and 81.4 fb^{-1} for $M = 4.0$, 4.5, 5.0, 5.5 and 6.0 TeV, respectively; for SSM Z' boson production, they are 0.015, 3.0 and 260 fb^{-1} for $M = 1$, 3 and 5 TeV; for graviton production, most of the interesting region of the (mass, coupling) plane is already covered with 10 fb^{-1}.

For KK Z and Z' production, a K factor of 1 was taken for both the signal and the Drell-Yan background, since heavy Z production interferes with Z/γ Drell-Yan production. For the graviton analysis, as little interference is present with the Standard Model processes, a K factor of 1.0 is used for the signal and of 1.3 for the Drell-Yan background, in order to take into account the higher order terms in the cross section. The latter number comes from the CDF analysis [111] and is compatible with the K factor obtained from theoretical computations [112, 113].

8.4.4 Systematic uncertainties

The uncertainty coming from the choice of the parton distribution function (PDF) was investigated using the set of 20 positive and 20 negative errors, of the CETQ6.1M "best fit" parameterization [114–116]. For each event, a weight factor is computed according to the x_1, x_2, and Q^2 variables, for each of the 40 PDF errors, in the case of graviton production with $M = 1.5$ TeV ($c = 0.01$) and $M = 3.5$ TeV ($c = 0.1$). The uncertainties on the PDF modify the number of signal events by a factor 1.20 (positive deviations) and 0.86 (negative deviations) for $M = 1.5$ TeV ($c = 0.01$). The corresponding numbers for $M = 3.5$ TeV ($c = 0.1$) are 1.47 and 0.78. For the Drell-Yan background, the re-weighting effects

Table 8.8: Number of events for resonant signal, $N_{\rm s}$, and for Drell-Yan background, $N_{\rm b}$, and corresponding significances as defined by Eq. 8.32, for an integrated luminosity of 30 fb^{-1}. The masses M and the mass windows $M_{\rm w}$ are in TeV.

	KK Z		SSM Z'		G, $c = 0.01$	G, $c = 0.1$
M	4.0	6.0	1.0	5.0	1.5	3.5
$M_{\rm w}$	3.5-4.5	5.0-6.7	0.92-1.07	4.18-5.81	1.47-1.52	3.30-3.65
$N_{\rm s}$	50.6	1.05	72020	0.58	18.8	7.30
$N_{\rm b}$	0.13	0.005	85.5	0.025	4.16	0.121
S	22.5	3.0	225	1.63	6.39	6.83

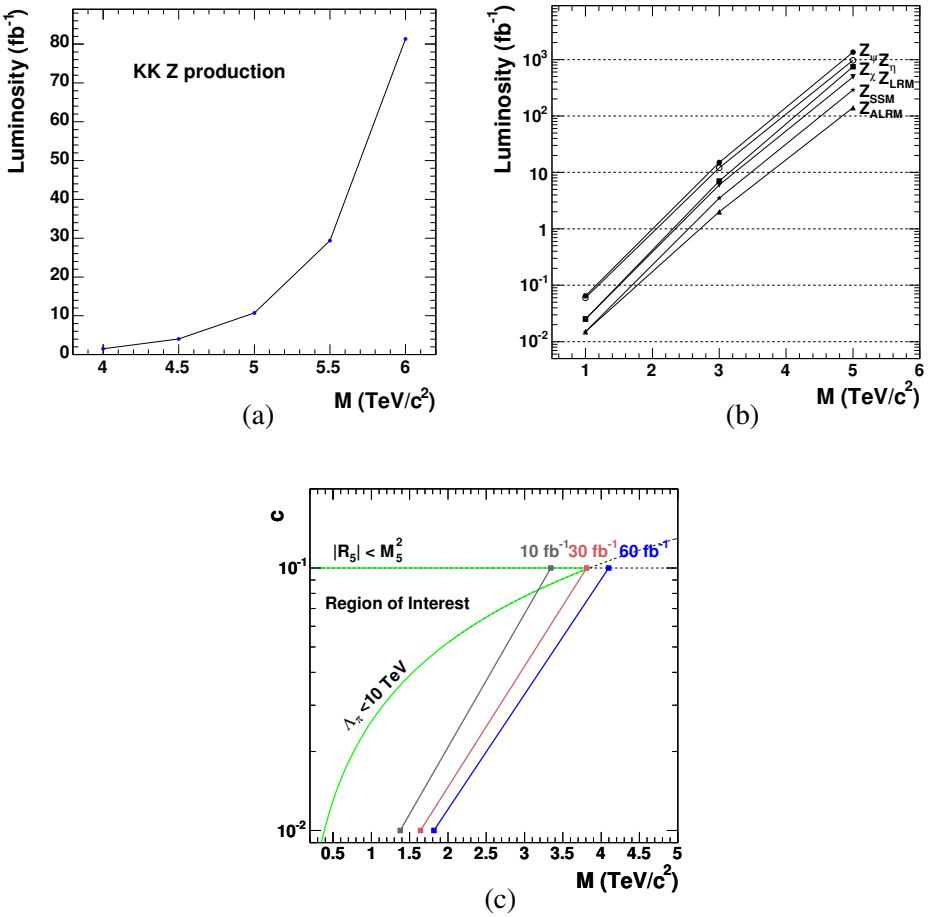

Fig. 8.13: 5σ discovery limit as a function of the resonance mass for KK Z boson production (a), for the 6 Z' models (b); 5σ discovery plane for graviton production as a function of the coupling parameter c and the graviton mass (c).

Table 8.9: The 5σ discovery limit on the resonance mass (given in TeV), for an integrated luminosity of 10, 30 and 60 fb^{-1}.

Model	Luminosity (fb^{-1})		
	10	30	60
KK Z	4.97	5.53	5.88
Z' (ψ)	2.85	3.31	3.62
Z' (ALRM)	3.76	4.27	4.60
G ($c = 0.01$)	1.38	1.64	1.82
G ($c = 0.1$)	3.34	3.81	4.10

on the numbers of events are 1.065 and 0.941 for masses around 1.5 TeV , and 1.19 and 0.88 for masses around 3.5 TeV. For an integrated luminosity of 30 fb^{-1}, the significances with the "best fit" and with the positive/negative deviations are equal respectively to 6.40 and 7.25/5.78 for $M = 1.5$ TeV ($c = 0.01$), and to 6.83 and 8.54/5.93 for $M = 3.5$ TeV ($c = 0.1$). A lower dependence is observed for the KK Z and Z' channels, which are produced by quark-antiquark annihilation. For KK Z boson production at $M = 4$ TeV with an integrated luminosity of 30 fb^{-1}, the significances with the "best fit" and with the positive/negative errors are equal respectively to 22.5 and 23.3/21.9.

Changing to 1 the value of the K factor of the DY background for RS graviton production increases the significance from 6.39 to 6.87 ($M = 1.5$ TeV , $c = 0.01$) and from 6.83 to 7.09 ($M = 3.5$ TeV , $c = 0.1$). The discovery limits increase respectively from 1.64 to 1.68 TeV and from 3.81 to 3.84 TeV.

8.4.5 Identification of new particles

Once a resonance is found, information will be gained on its characterization from the study of other decay channels, like $\gamma\gamma$ (see Section 9.5), of angular distributions and of asymmetries, in view of the spin determination (see also [117]).

As an example, RS gravitons with spin 2 can be distinguished from the Standard Model background and Z' bosons with spin 1 using the distribution of the $\cos\theta^*$ variable, computed as the cosine of the polar angle between the electron and the boost direction of the heavy particle in the latter rest frame. In addition to the cuts defined above, the electron and positron candidates are requested to have opposite charges, in order to identify the electron, from which the $\cos\theta^*$ variable is computed.

The $\cos\theta^*$ distributions for graviton production with M = 1.25 TeV, $c = 0.01$, and $M = 2.5$ TeV, $c = 0.1$, are presented in Fig. 8.14, for an integrated luminosity of 100 fb^{-1}. The error bars represent the corresponding statistical uncertainties, applied to the signal distribution obtained from a large statistics simulation. The spin-2 hypothesis is compared to the spin-1 hypothesis (red curve in the figures), formed by the Drell-Yan production (Figs. 8.14(a) and (b)) or the ALRM Z' production (Figs. 8.14(c) and (d)). For graviton production, the expected background is included in the $\cos\theta^*$ distributions.

The spin 2 of RS gravitons can be determined by contrast with the Drell-Yan production or the Z' boson production for an integrated luminosity of 100 fb^{-1} up to 1.25 TeV for $c = 0.01$ and 2.5 TeV for $c = 0.1$.

REFERENCES

[1] N. Arkani-Hamed, S. Dimopoulos and G. R. Dvali, Phys. Lett. **B429**, 263 (1998), [hep-ph/9803315].

[2] I. Antoniadis, N. Arkani-Hamed, S. Dimopoulos and G. R. Dvali, Phys. Lett. **B436**, 257 (1998), [hep-ph/9804398].

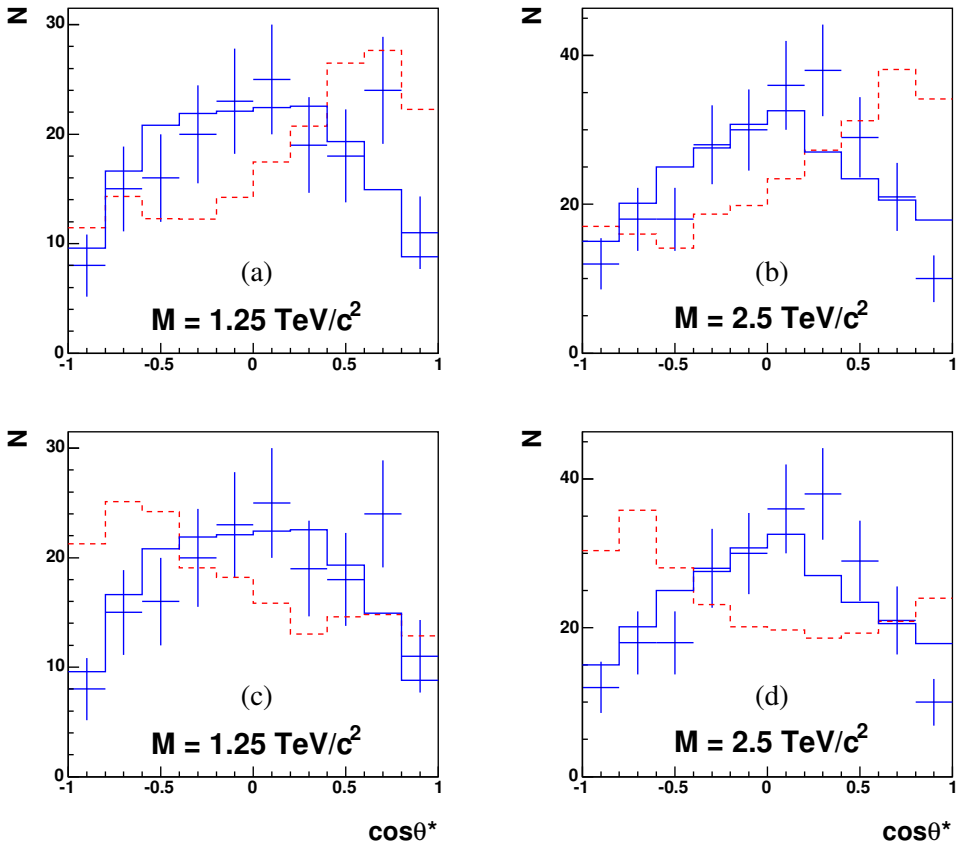

Fig. 8.14: Distributions of $\cos\theta^*$ for graviton production (blue curves) and for Drell-Yan production (red curves) normalized to the signal, for M = 1.25 TeV (a) and 2.5 TeV (b), and for Z' boson (ALRM model) (red curves), normalized to the signal, for M = 1.25 TeV (c) and 2.5 TeV (d), with an integrated luminosity of 100 fb^{-1}. The error bars represent the "1-experiment" distribution for the graviton production. For graviton production, the expected background is included in the $\cos\theta^*$ distributions.

[3] L. Randall and R. Sundrum, Phys. Rev. Lett. **83**, 3370 (1999), [hep-ph/9905221].

[4] L. Randall and R. Sundrum, Phys. Rev. Lett. **83**, 4690 (1999), [hep-th/9906064].

[5] C. D. Hoyle *et al.*, Phys. Rev. **D70**, 042004 (2004), [hep-ph/0405262].

[6] I. Antoniadis, Phys. Lett. **B246**, 377 (1990).

[7] A. Hebecker and J. March-Russell, Nucl. Phys. **B625**, 128 (2002), [hep-ph/0107039].

[8] C. Csaki, C. Grojean, H. Murayama, L. Pilo and J. Terning, Phys. Rev. **D69**, 055006 (2004), [hep-ph/0305237].

[9] N. Arkani-Hamed and M. Schmaltz, Phys. Rev. **D61**, 033005 (2000), [hep-ph/9903417].

[10] T. Appelquist, H.-C. Cheng and B. A. Dobrescu, Phys. Rev. **D64**, 035002 (2001), [hep-ph/0012100].

[11] T. Flacke, D. Hooper and J. March-Russell, hep-ph/0509352.

[12] H.-C. Cheng, J. L. Feng and K. T. Matchev, Phys. Rev. Lett. **89**, 211301 (2002), [hep-ph/0207125].

[13] G. Servant and T. M. P. Tait, Nucl. Phys. **B650**, 391 (2003), [hep-ph/0206071].

[14] P. Nath and M. Yamaguchi, Phys. Rev. **D60**, 116004 (1999), [hep-ph/9902323].

[15] M. Masip and A. Pomarol, Phys. Rev. **D60**, 096005 (1999), [hep-ph/9902467].

[16] T. G. Rizzo and J. D. Wells, Phys. Rev. **D61**, 016007 (2000), [hep-ph/9906234].

[17] A. Strumia, Phys. Lett. **B466**, 107 (1999), [hep-ph/9906266].

[18] R. Casalbuoni, S. De Curtis, D. Dominici and R. Gatto, Phys. Lett. **B462**, 48 (1999), [hep-ph/9907355].

[19] A. Delgado, A. Pomarol and M. Quiros, JHEP **01**, 030 (2000), [hep-ph/9911252].

[20] A. Muck, A. Pilaftsis and R. Ruckl, Phys. Rev. **D65**, 085037 (2002), [hep-ph/0110391].

[21] A. Muck, A. Pilaftsis and R. Ruckl, hep-ph/0210410.

[22] G. F. Giudice, R. Rattazzi and J. D. Wells, Nucl. Phys. **B544**, 3 (1999), [hep-ph/9811291].

[23] T. Han, J. D. Lykken and R.-J. Zhang, Phys. Rev. **D59**, 105006 (1999), [hep-ph/9811350].

[24] N. Arkani-Hamed, S. Dimopoulos and J. March-Russell, Phys. Rev. **D63**, 064020 (2001), [hep-th/9809124].

[25] The LEP Exotica Working Group, LEP Exotica WG note 2004-03, see also `http://lepexotica.web.cern.ch/lepexotica`.

[26] V. M. Abazov *et al.* (D0 Collaboration), Phys. Rev. Lett. **90**, 251802 (2003), [hep-ex/0302014].

[27] D. Acosta (CDF Collaboration), Phys. Rev. Lett. **92**, 121802 (2004), [hep-ex/0309051].

[28] S. Hannestad and G. G. Raffelt, Phys. Rev. Lett. **88**, 071301 (2002), [hep-ph/0110067].

[29] S. Hannestad and G. G. Raffelt, Phys. Rev. **D67**, 125008 (2003), [hep-ph/0304029].

[30] M. Spiropulu, hep-ex/0505003.

[31] G. F. Giudice, T. Plehn and A. Strumia, Nucl. Phys. **B706**, 455 (2005), [hep-ph/0408320].

[32] G. F. Giudice, R. Rattazzi and J. D. Wells, Nucl. Phys. **B595**, 250 (2001), [hep-ph/0002178].

[33] L. Vacavant and I. Hinchliffe, J. Phys. **G27**, 1839 (2001).

[34] J. A. Aguilar-Saavedra *et al.* (ECFA/DESY LC Physics Working Group), hep-ph/0106315.

[35] G. W. Wilson, LC-PHSM-2001-010, Feb. 2001.

[36] M. Battaglia, D. Dominici and J. F. Gunion, hep-ph/0402062.

[37] T. Han, D. L. Rainwater and D. Zeppenfeld, Phys. Lett. **B463**, 93 (1999), [hep-ph/9905423].

[38] V. Kabachenko, A. Miagkov and A. Zenin (ATLAS Collaboration), (2001), ATL-PHYS-2001-012.

[39] J. L. Hewett, Phys. Rev. Lett. **82**, 4765 (1999), [hep-ph/9811356].

[40] T. G. Rizzo, JHEP **10**, 013 (2002), [hep-ph/0208027].

[41] T. G. Rizzo, JHEP **02**, 008 (2003), [hep-ph/0211374].

[42] P. Osland, A. A. Pankov and N. Paver, Phys. Rev. **D68**, 015007 (2003), [hep-ph/0304123].

[43] A. A. Pankov and N. Paver, Phys. Rev. **D72**, 035012 (2005), [hep-ph/0501170].

[44] A. A. Pankov and N. Paver, hep-ph/0508174.

[45] E. Accomando *et al.* (CLIC Physics Working Group), hep-ph/0412251.

[46] J. D. Wells, hep-ph/0205328.

[47] M. Battaglia, D. Dominici, J. F. Gunion and J. D. Wells, hep-ph/0402062.

[48] S. Abdullin *et al.*, Eur. Phys. J. **C39S2**, 41 (2005).

[49] G. F. Giudice and A. Strumia, Nucl. Phys. **B663**, 377 (2003), [hep-ph/0301232].

[50] A. Datta, K. Huitu, J. Laamanen and B. Mukhopadhyaya, Phys. Rev. **D70**, 075003 (2004), [hep-ph/0404056].

[51] N. Arkani-Hamed, S. Dimopoulos and G. R. Dvali, Phys. Rev. **D59**, 086004 (1999), [hep-ph/9807344].

[52] H.-C. Cheng, K. T. Matchev and M. Schmaltz, Phys. Rev. **D66**, 056006 (2002), [hep-ph/0205314].

[53] H.-C. Cheng, K. T. Matchev and M. Schmaltz, Phys. Rev. **D66**, 036005 (2002), [hep-ph/0204342].

[54] A. Pomarol and M. Quiros, Phys. Lett. **B438**, 255 (1998), [hep-ph/9806263].

[55] I. Antoniadis, K. Benakli and M. Quiros, Phys. Lett. **B460**, 176 (1999), [hep-ph/9905311].

[56] K. Cheung and G. Landsberg, Phys. Rev. **D65**, 076003 (2002), [hep-ph/0110346].

[57] I. Antoniadis, K. Benakli and M. Quiros, Phys. Lett. **B331**, 313 (1994), [hep-ph/9403290].

[58] E. Accomando, I. Antoniadis and K. Benakli, Nucl. Phys. **B579**, 3 (2000), [hep-ph/9912287].

[59] N. Arkani-Hamed, S. Dimopoulos, G. R. Dvali and J. March-Russell, Phys. Rev. **D65**, 024032 (2002), [hep-ph/9811448].

[60] F. de Campos, M. A. Garcia-Jareno, A. S. Joshipura, J. Rosiek and J. W. F. Valle, Nucl. Phys. **B451**, 3 (1995), [hep-ph/9502237].

[61] A. S. Joshipura and S. D. Rindani, Phys. Rev. Lett. **69**, 3269 (1992).

[62] A. S. Joshipura and J. W. F. Valle, Nucl. Phys. **B397**, 105 (1993).

[63] J. McDonald, Phys. Rev. **D50**, 3637 (1994).

[64] C. P. Burgess, M. Pospelov and T. ter Veldhuis, Nucl. Phys. **B619**, 709 (2001), [hep-ph/0011335].

[65] H. Davoudiasl, R. Kitano, T. Li and H. Murayama, Phys. Lett. **B609**, 117 (2005), [hep-ph/0405097].

[66] M. I. Josa (ALEPH, DELPHI, L3 and OPAL Collaborations), Prepared for International Europhysics Conference on High-Energy Physics (HEP 2001), Budapest, Hungary, 2001, see: `jhep.sissa.it/archive/prhep/preproceeding/007/145/higgs.pdf`.

[67] J. F. Gunion, Phys. Rev. Lett. **72**, 199 (1994), [hep-ph/9309216].

[68] D. Choudhury and D. P. Roy, Phys. Lett. **B322**, 368 (1994), [hep-ph/9312347].

[69] S. G. Frederiksen, N. Johnson, G. L. Kane and J. Reid, Phys. Rev. **D50**, 4244 (1994).

[70] O. J. P. Eboli and D. Zeppenfeld, Phys. Lett. **B495**, 147 (2000), [hep-ph/0009158].

[71] B. P. Kersevan, M. Malawski and E. Richter-Was, Eur. Phys. J. **C29**, 541 (2003), [hep-ph/0207014].

[72] D. Cavalli *et al.*, The Higgs Working Group: summary report (2001), in the proceedings of Workshop on Physics at TeV Colliders, Les Houches, 2001, hep-ph/0203056.

[73] R. M. Godbole, M. Guchait, K. Mazumdar, S. Moretti and D. P. Roy, Phys. Lett. **B571**, 184 (2003), [hep-ph/0304137].

[74] K. Belotsky, V. A. Khoze, A. D. Martin and M. G. Ryskin, Eur. Phys. J. **C36**, 503 (2004), [hep-ph/0406037].

[75] H. Davoudiasl, T. Han and H. E. Logan, Phys. Rev. **D71**, 115007 (2005), [hep-ph/0412269].

[76] V. D. Barger, R. J. N. Phillips and D. Zeppenfeld, Phys. Lett. **B346**, 106 (1995), [hep-ph/9412276].

[77] D. L. Rainwater, *Intermediate-mass Higgs searches in weak boson fusion*, Ph.D. thesis, University of Wisconsin, Madison, 1999, hep-ph/9908378,

[78] S. P. Martin and J. D. Wells, Phys. Rev. **D60**, 035006 (1999), [hep-ph/9903259].

[79] T. Han and S. Willenbrock, Phys. Lett. **B273**, 167 (1991).

[80] O. Brein, A. Djouadi and R. Harlander, Phys. Lett. **B579**, 149 (2004), [hep-ph/0307206].

[81] J. Ohnemus and J. F. Owens, Phys. Rev. **D43**, 3626 (1991).

[82] J. M. Campbell and R. K. Ellis, Phys. Rev. **D60**, 113006 (1999), [hep-ph/9905386].

[83] O. Brein *et al.*, Precision calculations for associated W H and Z H production at hadron colliders, Contributed to 3rd Les Houches Workshop: Physics at TeV Colliders, Les Houches, France, 26 May - 6 Jun 2003, hep-ph/0402003.

[84] M. Dührssen, Prospects for the measurement of Higgs boson coupling parameters in the mass range from 110–190 GeV, ATL-PHYS-2003-030.

[85] T. Figy, C. Oleari and D. Zeppenfeld, Phys. Rev. **D68**, 073005 (2003), [hep-ph/0306109].

[86] E. L. Berger and J. Campbell, Phys. Rev. **D70**, 073011 (2004), [hep-ph/0403194].

[87] R. E. Shrock and M. Suzuki, Phys. Lett. **B110**, 250 (1982).

[88] A. Nikitenko and K. Mazumdar, Observation of Invisible Decay Mode of Higgs Boson at CMS, CMS IN-2004/028.

[89] T. Sjostrand, L. Lonnblad and S. Mrenna, hep-ph/0108264.

[90] M. Spira, A. Djouadi, D. Graudenz and P. M. Zerwas, Nucl. Phys. **B453**, 17 (1995), [hep-ph/9504378].

[91] K. Cranmer, T. Figy, W. Quayle, D. Rainwater and D. Zeppenfeld, Madison Collection of User Processes.

[92] K. Hagiwara and D. Zeppenfeld, Nucl. Phys. **B313**, 560 (1989).

[93] A. Pukhov *et al.*, hep-ph/9908288.

[94] F. Maltoni and T. Stelzer, JHEP **02**, 027 (2003), [hep-ph/0208156].

[95] M. L. Mangano, M. Moretti, F. Piccinini, R. Pittau and A. D. Polosa, JHEP **07**, 001 (2003), [hep-ph/0206293].

[96] CMS Collaboration, CMS Simulation Package.

[97] CMS Collaboration, Object-oriented reconstruction for CMS analysis, CMS Physics TDR Volume 1.

[98] K. A. Abdullin S and S. N, Cmsjet, 1994, CMS TN/94-180.

[99] CMS Collaboration, The data acquisition and high-level trigger project, 2002, CMS TDR 2002/6.1.

[100] B. Di Girolamo, A. Nikitenko, L. Neukermans, K. Mazumdar and D. Zeppenfeld, Experimental observation of an invisible Higgs boson at LHC, in: Workshop on Physics at TeV Colliders, Les Houches, France, 21 May - 1 Jun 2001.

[101] K. R. Dienes, E. Dudas and T. Gherghetta, Nucl. Phys. **B537**, 47 (1999), [hep-ph/9806292].

[102] J. L. Rosner, Phys. Rev. **D35**, 2244 (1987).

[103] M. Cvetic and S. Godfrey, hep-ph/9504216.

[104] S. Godfrey, Proc. Snowmass 2001, Snowmass Village, CO, 2001, eConf **C010630**, P344 (2001), [hep-ph/0201093].

[105] Particle Data Group, S. Eidelman *et al.*, Phys. Lett. **B592**, 1 (2004).

[106] B. Clerbaux, T. Mahmoud, C. Collard and P. Miné, CMS Note 2006-083 (2006).

[107] C. Collard and M.-C. Lemaire, CMS Note 2004-024 (2004).

[108] D. Acosta *et al.* (CMS Collaboration), CERN/LHCC 2006-001 (2006).

[109] B. Clerbaux, T. Mahmoud, C. Collard, M.-C. Lemaire and V. Litvin, CMS Note 2006-004 (2006).

[110] V. Bartsch and G. Quast, CMS Note 2005-004 (2005).

[111] T. Affolder *et al.* (CDF Collaboration), Phys. Rev. Lett. **87**, 131802 (2001).

[112] R. Hamberg, W. L. van Neerven and T. Matsuura, Nucl. Phys. **B359**, 343 (1991).

[113] R. Hamberg, W. L. van Neerven and T. Matsuura, Nucl. Phys. **B644**, 403 (2002).

[114] H. L. Lai *et al.* (CTEQ Collaboration), Eur. Phys. J. **C12**, 375 (2000), [hep-ph/9903282].

[115] J. Pumplin *et al.* (CTEQ Collaboration), JHEP **0207**, 012 (2002), [hep-ph/0201195].

[116] D. Stump *et al.* (CTEQ Collaboration), JHEP **0310**, 046 (2003), [hep-ph/0303013].

[117] R. Cousins, J. Mumford and V. Valuev, CMS Note 2005-022 (2005).